Characterization and antibacterial effect of modified polymer surfaces

Bačeković, Marija

University of Split
Faculty of Science

Characterization and antibacterial effect of modified polymer surfaces

Master thesis

Marija Bačeković

Split, december 2023.

Temeljna dokumentacijska kartica

Sveučilište u Splitu
Prirodoslovno–matematički fakultet
Odjel za fiziku
Ruđera Boškovića 33, 21000 Split, Hrvatska

Diplomski rad

Karakterizacija i antibakterijski efekt modificiranih polimernih površina

Marija Bačeković

Sveučilišni diplomski studij Fizika, smjer Biofizika

Sažetak:

U ovom radu istražuju se morfološka svojstva polimera s površinskim modifikacijama koje potiču antibakterijski učinak. Četiri uobičajena polimera prošla su detaljnu morfološku analizu pomoću skenirajućeg elektronskog mikroskopa (eng. SEM - *scanning electron microscope*). Fokusirajući se na PET (eng. *Polyethylene Terephthalat*) i HDPE (eng. *High-Density Polyethylene*), oba su polimera podvrgnuta tretmanu putem atmosferskog plazmenog mlaza kako bi se povećala hrapavost površine. Naknadno poboljšanje koloidima Ag i ZnO ispitano je pomoću SEM-a. Energijski razlučujuća rendgenska spektroskopija (eng. EDS - *energy dispersive spectroscopy*) omogućila je uvid u atomski sastav, dok je mikroskopija atomskih sila (eng. AFM - *atomic force microscopy*) mjerila hrapavost površine. Zbog izazova koje predstavlja nevodljivost i malena hrapavost površine, SEM mjerenje je provedeno s niskim ubrzavajućim naponom na obloženim uzorcima. Primijećeno je znatno povećanje hrapavosti nakon obrade mlazom plazme te su nanočestice uspješno izmjerene. Uzorci obogaćeni koloidima su pokazali određenu antibakterijsku efikasnost. Daljnja istraživanja trebala bi se usmjeriti na poboljšanje antibakterijskog učinka i njegovog protokola testiranja.

Ključne riječi: polimeri, atmosferski plazmeni mlaz, nanočestice, skenirajući elektronski mikroskop, energijski razlučujuća rendgenska spektroskopija, mikroskopija atomskih sila, antibakterijski efekt

Rad sadrži: 49 stranica, 33 slike, 3 tablice, 12 literaturnih navoda. Izvornik je na engleskom jeziku.

Mentor: doc. dr. sc. Lucija Krce

Ocjenjivači: doc. dr. sc. Lucija Krce,
prof. dr. sc. Ante Bilušić,
doc. dr. sc. Ivana Weber

Rad prihvaćen: 21.12.2023.

Rad je pohranjen u Knjižnici Prirodoslovno–matematičkog fakulteta, Sveučilišta u Splitu.

Basic documentation card

University of Split
Faculty of Science
Department of Physics
Ruđera Boškovića 33, 21000 Split, Croatia

Master thesis

Characterization and antibacterial effect of modified polymer surfaces

Marija Bačeković

University graduate study Physics, specialization in Biophysics

Abstract:

This thesis investigates the morphological characteristics of polymers with surface modifications that promote antibacterial effect. Four common polymers underwent detailed morphological analysis using a scanning electron microscope (SEM). Focusing on PET and HDPE, both polymers underwent Atmospheric pressure plasma jet treatment for increased surface roughness. Subsequent enhancement with Ag and ZnO colloids was examined using SEM. EDS analysis provided insights into atomic composition, while AFM measured surface roughness. Because of the challenges posed by non-conductivity and low surface roughness, SEM imaging was conducted with low accelerating voltage on coated samples. Notably, an increase in roughness post plasma jet treatment was observed and nanoparticles were successfully imaged. Antibacterial efficacy, evaluated against *S. aureus*, indicated a observable effect in colloidal-enhanced samples. Further research should address improvement of the antibacterial effect and its testing protocol.

Keywords: polymers, atmospheric pressure plasma jet, nanoparticles, scanning electron microscope, energy dispersive spectroscopy, atomic force microscopy, antibacterial effect

Thesis consists of: 49 pages, 33 figures, 3 tables, 12 references. Original language: English.

Supervisor: Assist. Prof. Dr. Lucija Krce

Reviewers: Assist. Prof. Dr. Lucija Krce,
Prof. Dr. Ante Bilušić,
Assist. Prof. Dr. Ivana Weber

Thesis accepted: December 21, 2023.

Thesis is deposited in the library of the Faculty of Science, University of Split.

I would like to thank my mentor, Assist. Prof. Dr. Lucija Krce, for her expert and patient guidance. Your enthusiastic approach to research and science left a lasting impression on me and I thank you for the privilege of being your mentee.

My thanks also goes to Prof. Dr. Ante Bilušić, on whose advice I could always count on when there were problems that seemed unsolvable. Thank you for your time and effort.

Thank you to my colleagues from Institute of Physics, Assist. Prof. Dr. Nikša Krastulović and mag. phys. Rafaela Radičić, who are a part of the HrZZ IP-2019-04-6418 project, for preparing the samples used and for answering any and all questions about their research and literature.

Also, thank you to mag. educ. biol. et chem. Doris Crnčević, for the help and patience in preparing the samples for antibacterial protocol.

And lastly, thank you to my family and friends for their patience and support. To my mother, for being my biggest rock to lean on and the most enthusiastic cheerleader that one can hope to have. Your continual belief in me inspired everything I am. To Ante, thank you for letting me pursue my dreams and supporting me on this path I have chosen. You always believed that I will find my way. And to Noa, my love for you made me a better and more patient person, as well as the most efficient student, all so I can come back home to you as quickly as possible.

Contents

1 Introduction

Polymers, as relatively inexpensive materials, can undergo enhancement of their physical and chemical attributes through alterations in surface properties or the impregnation of metal nanoparticles. The resulting polymer/nanoparticle hybrid materials showcase outstanding properties applicable across diverse domains like nanobiotechnology, nanobiomedicine, and the food industry. The atmospheric pressure plasma jet serves to enhance the surface roughness of treated samples, facilitating easier embedding of nanoparticles. On the other hand, metal nanoparticles showcase antibacterial activity, disrupting bacterial cell membranes, interfering with cellular respiration, disrupting DNA replication and cellular processes. The aim of this work is to investigate the antibacterial potential of common materials treated with plasma and enhanced with nanoparticles. This thesis explores the morphological characteristics of polymers with such surface modifications. The study encompasses four common polymers — Polyethylene Terephthalate (PET), High-Density Polyethylene (HDPE), Low-Density Polyethylene (LDPE) and Polystyrene (PS) — whose morphological features were meticulously examined using a scanning electron microscope (SEM) at high magnifications. The research then delves deeper into the morphological attributes of PET and HDPE. In light of their considerable smoothness, both polymers underwent Atmospheric pressure plasma jet (APPJ) treatment to achieve rougher surfaces. Subsequently, the samples were enhanced with Ag and ZnO nanoparticles, and the resulting surfaces were scrutinized using SEM. APPJ treatment and nanoparticle enhancement was done by our colleagues from Institute of Physics, Assist. Prof. Dr. Nikša Krstulović and mag. phys. Rafaela Radičić. Further insights into the atomic composition were obtained through energy dispersive X-ray spectroscopy, while imaging with atomic force microscope was employed to assess surface roughness. The conclusive phase of the research involved evaluating the antibacterial efficacy of each sample against a representative strain of bacteria *S. aureus*.

2 Scanning electron microscope

Since its introduction and commercial application in 1967, the scanning electron microscope (SEM) has undergone significant advancements, expanding its capabilities in material studies. The evolution of instrumentation and computer technology has enabled the SEM to reveal surface morphology at scales ranging from micrometers to nanometers. Renowned for its versatility, simplicity, and efficacy in sample preparation and result interpretation, the scanning electron microscope has become a potent tool for diverse analyses, encompassing microchemical to crystallographic investigations. Like all microscopes, the primary role of the SEM is to magnify small features and objects imperceptible to the naked eye. This is achieved through a high-energy electron beam that scans the sample's surface. The SEM's superior resolution, attributable to the electron's shorter wavelength compared with visible photons used in optical microscopy, allows for detailed imaging. [2]

The scanning electron microscope comprises three main components: the electron column, the sample chamber, and computer/electronic controls (Figure 1). The upper section of the electron column features an electron gun producing the electron beam. Electromagnetic lenses within the column focus the beam into a probe with a small diameter, while scanning coils move the probe across the sample's surface. The electron beam can penetrate up to several micrometers into the sample, interacting with its atoms and resulting in backscattered and secondary electrons, as well as characteristic X-rays. These signals may be collected and processed to generate images and reveal the composition of the sample surface.

SEM finds applications in examining the surface details of diverse materials, including metals, alloys, ceramics, polymers, membranes, fractured/rough surfaces, and biological samples. It accommodates conductive or non-conductive materials in solid or powder form, allowing examination in their received or prepared states. Noteworthy is its capability to display a substantial depth of field (10–100% horizontal field of view), enabling large sample areas to remain in focus simultaneously and offering three-dimensional characteristics in SEM images.

Despite its numerous advantages, SEM does have limitations. Notably, samples must be in a solid state and of limited size, measuring must occur under vacuum conditions, the instrument typically requires a 5 m $\times$ 5 m installation space, and non-conductive samples must undergo coating with a metallic layer. [1]

2.1 Components of the SEM

As previously mentioned, the scanning electron microscope's primary components are an electron column, a sample chamber, and a computer control system. The SEM instrumentation may incorporate various detectors for secondary and backscattered electrons, such as energy

Figure 1: *Field Emission Scanning Electron Microscope, JEOL JSM-7610FPlus, used in our research. Primary components are labeled as follows: (1) electron column, (2) sample chamber, (3) computer control system.*

dispersive X-ray spectrometer (EDS), cathodoluminescence detector that measures photons from the ultraviolet to the near infrared range, wavelength dispersive X-ray spectrometer, an electron backscattered diffraction (EBSD) detector, etc. While some of these instruments may not be necessary for basic imaging, they become increasingly crucial for more intricate microscopic applications. The user maintains continuous interaction with the SEM's primary components, with input parameters determined by the operator directly impacting the quality of acquired images and analyses.

Apart from these core components, secondary and miscellaneous equipment, including vacuum pumps, water coolers, and electronics, form an integral part of the overall system. Without this equipment, the SEM would be unable to function. Nevertheless, these supporting elements operate seamlessly in the background, requiring minimal input from the user. [1]

2.1.1 Electron column

Situated above the sample chamber, the electron column of the SEM takes the form of a lengthy cylindrical structure. It contains an electron gun, multiple electron lenses, scan coils, as well as condenser and objective apertures (depicted in schematic diagram in Figure 2). The electron column operates under a constant vacuum of the order of magnitude of 10^{-4} Pa.

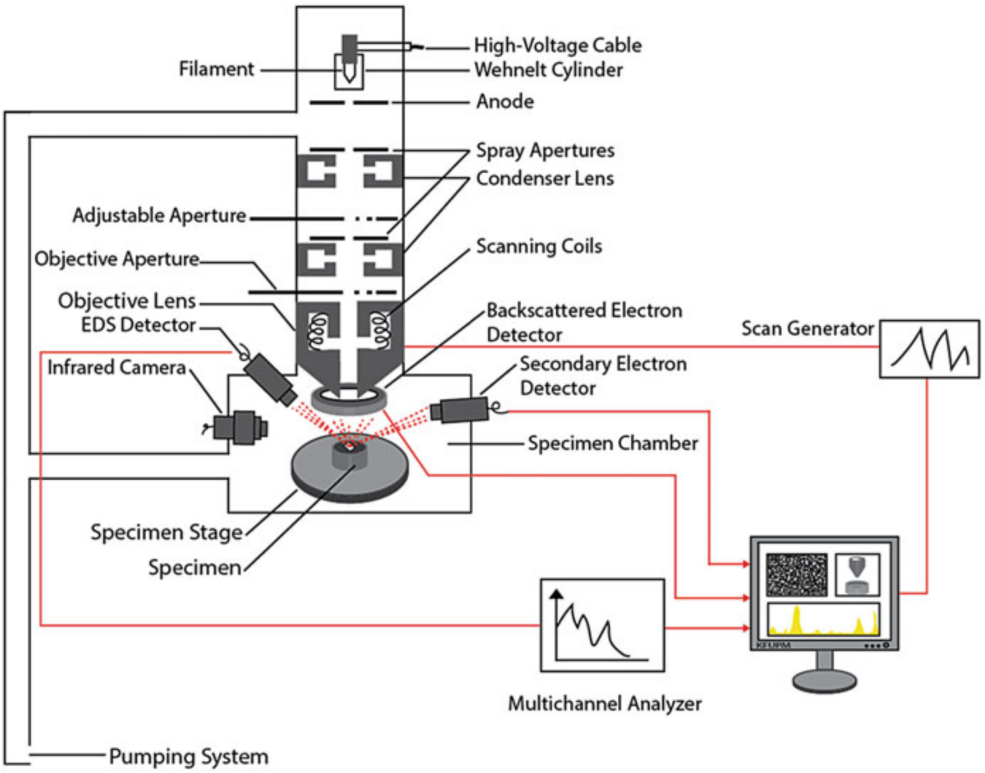

Figure 2: *Schematic diagram of the scanning electron microscope which has a tungsten electrode for an electron gun. [1]*

Occupying the upper portion of the column is the electron gun assembly, comprising the cathode and associated electrodes. This assembly is linked to a high-voltage power cable, typically operating within the range of 30-40 kV. The primary role of the electron gun is to generate electrons, which are subsequently propelled down the column due to the potential difference within the gun assembly. The force exerted by the electrons as they traverse the column and ultimately impact the sample is contingent upon factors such as the acceleration voltage used, the nature of the analysis, and the specific information sought. [1]

There are several different types of electron guns, the most important of which are *field emission gun* and *thermionic emission gun*.

In field emission electron guns, the cathode emitter takes the form of a sharp tip, and the emission of electrons occurs by applying a negative potential to the cathode's apex. This leads to a concentrated electric field in the vicinity of the small tip, resulting in a substantial reduction in the height of the potential barrier. The narrowed potential barrier allows electrons to overcome it through a phenomenon known as quantum tunneling, where a particle surpasses a potential barrier with energy lower than that of the particle itself. [1]

Two types of field-emission electron guns exist: the cold field-emission electron gun and the Schottky field-emission electron gun. The cold field-emission electron gun operates by extracting electrons through the tunnel effect from the surface of a tungsten cathode when a

strong electric field is applied at room temperature. On the other hand, the Schottky field-emission electron gun utilizes electric-field emission facilitated by the introduction of zirconium oxide to the tungsten surface, thereby lowering the tungsten's work function, W, which is defined as the minimum energy required to dislodge an electron from the surface of a given solid and propel it to infinity. In the JSM-7610FPlus, a Schottky field-emission electron gun is implemented, effectively reducing the work function of tungsten through the application of zirconium oxide (Figure 3). Unlike the cold field-emission electron gun, the Schottky variant can consistently supply the cathode surface with zirconium oxide by heating it to 1800 K. Consequently, the Schottky field-emission electron gun offers enhanced stability and a higher probe current compared to the traditional cold field-emission electron gun. [2]

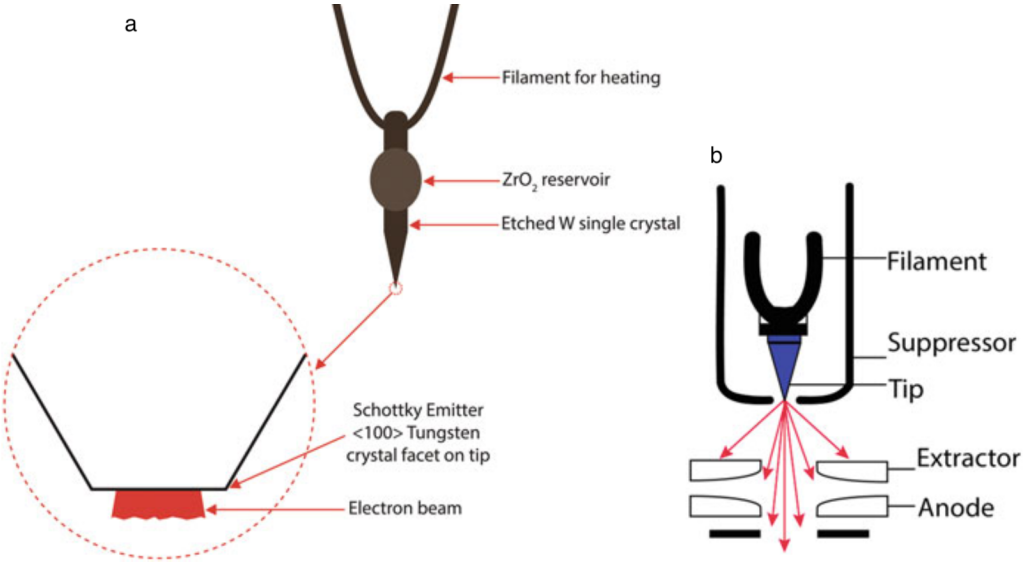

Figure 3: *(a) Schematic diagram of emission patterns from a Schottky emitter. (b) Schematic representation of Schottky field emission gun setup. [1]*

The process of generating electrons exploits the phenomenon of thermionic emission in a thermionic gun. The departure of electrons from a metal surface demands energy due to the attractive forces between positively charged nuclei and negatively charged electrons. Through adequate heating, certain electrons gain sufficient energy to surmount the inherent potential energy barrier preventing their release from the metal. Consequently, electron emission resulting from the heating of a material is termed thermionic emission, with the corollary that reducing the work function enhances the thermionic current. The Richardson-Dushman equation describes thermionic emission in the following manner:

$$J_e = \frac{\tau^2 me}{2\pi^2\hbar^3} e^{\left(\frac{-W}{\tau}\right)}, \tag{2.1}$$

where J_e is the emission current density, m and e mass and charge of the electron and $\tau = k_B T$ is the energy equivalent of the temperature of the metal.

The thermionic emission electron gun consists of three parts: emitter (cathode, negative

electrode), grounded plate (plate, positive electrode) and surrounding grid cover with a circular aperture (Wehnelt cylinder, control electrode). The emitter cathode is in the form of a filament whose tip is positioned at the center of the Wehnelt cylinder aperture (Figure 4).

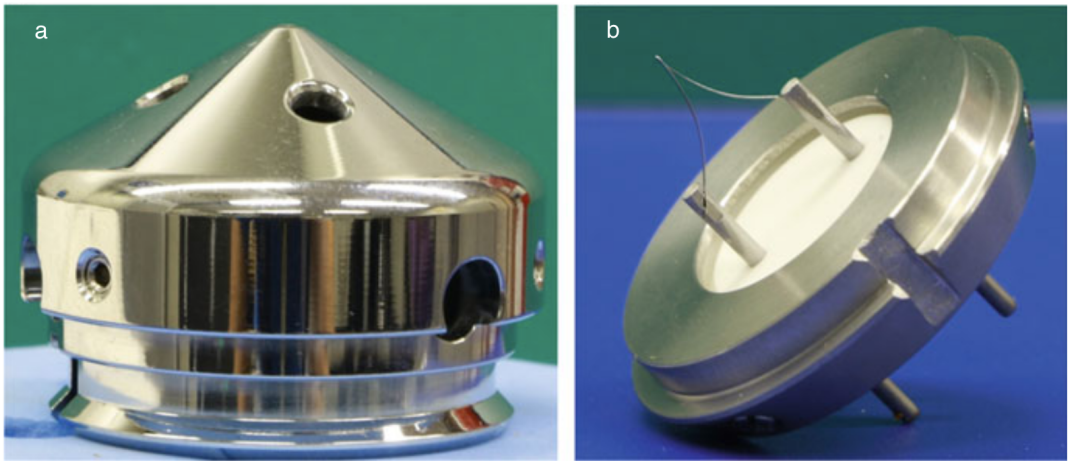

Figure 4: *Photographs of (a) Wehnelt cylinder and (b) W filament. By inserting the filament into the Wehnelt cylinder, these two components are combined to create a W filament gun. [1]*

Electrons overcome the work function of the filament and escape its surface when the filament is heated by a current. The anode is grounded at zero potential while the filament is kept at a high negative potential. This difference in potential accelerated the generated electrons downward through a hole in the anode toward the sample. The Wehnelt cylinder or the grid cover is kept at a negative bias of a few hundred volts relative to the cathode emitter and that bias serves to focus the generated electrons into a beam. This is how the triode gun serves as an electrostatic lens. [1]

2.1.2 Electromagnetic lenses

The scanning electron microscope's electron optical system shapes a precise electron probe that scans the specified area on the specimen in a raster pattern. In SEM, lenses play a crucial role in demagnifying or focusing the electron beam generated by the electron gun. This demagnification or re-convergence process involves typically two condenser lenses initially and a final objective lens, working together to create a fine probe on the specimen's surface. Electromagnetic lenses consist of a copper coil enclosed in an iron casing with a gap surrounded by cylindrical pole pieces, as depicted in the schematic illustration in Figure 5.

A concentrated magnetic field is generated by the direct current flowing through the coil and is confined within the iron casing, except for the gap between the lens pole pieces. This gap allows the magnetic field to exert force on the electrons traveling down the electron column. As an electron with charge e and velocity $\vec{v}$ passes through an electromagnetic lens, it experiences a force magnitude $\vec{F}$, determined by the concentrated magnetic field:

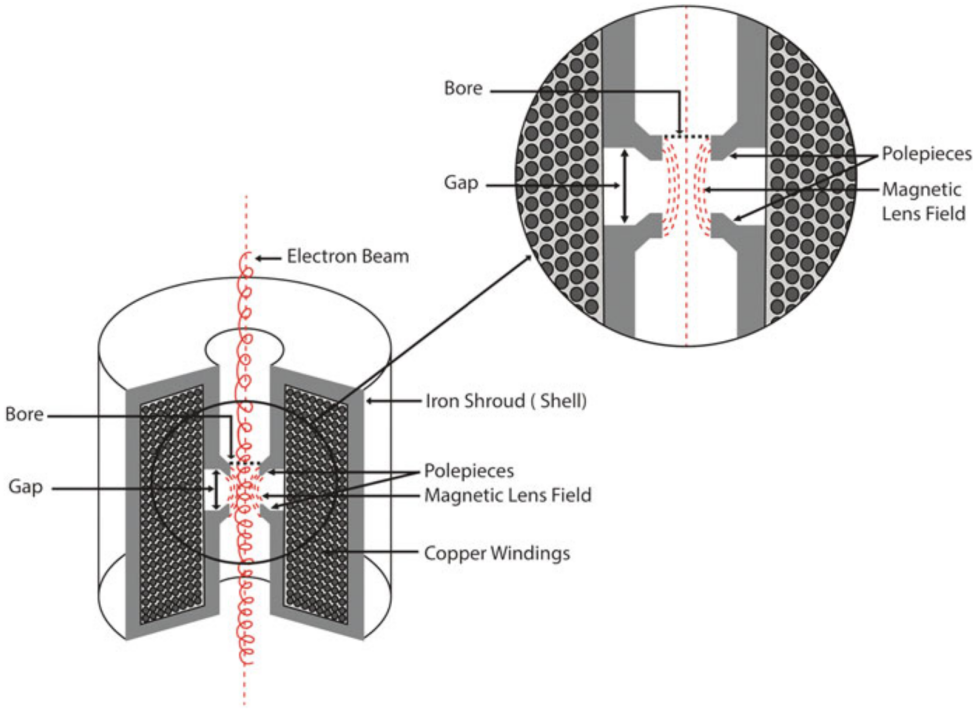

Figure 5: *Schematic illustration depicting an electromagnetic lens, where copper wires are enclosed within an iron shroud. The electromagnetic field interacts with the electron beam through the gap situated between the pole pieces. [1]*

$$\vec{F} = e\vec{B} \times \vec{v}, \tag{2.2}$$

where B is the magnetic field. The magnetic field has a radial B_R (perpendicular to the optic axis) and axial/longitudinal B_L (parallel to optic axis) component. The electrons emanating from gun that are off-axis interact with the radial field which causes them to spiral down in a helical path and deflects them toward the axis. The focusing effect is accomplished because the electrons away from the optic axis are deflected with greater force compared to the ones that are closer (Figure 6). [1]

Condenser lens (two to three) can be present directly below the electron gun and they demagnify the electron beam diameter by regulating the current in the lens coils. Strong lens with strong focusing action, for example electrons focused closer to the lens or small focal length, are achieved by increasing the current of the lens coil.

When there is a strong condenser, it spreads out the electrons in a way that a large number of them are blocked by the aperture and do not reach the next lens. The result is a small probe size and current on the specimen (Figure 7 (b)). Weak lens with weak focusing action, for example electrons focused away from the lens or long focal length, are therefore achieved by decreasing the current in the lens coil. The trajectory of electrons through is unobstructed and a large number of them reach the second lens which results in a large current and spot size (Figure 7

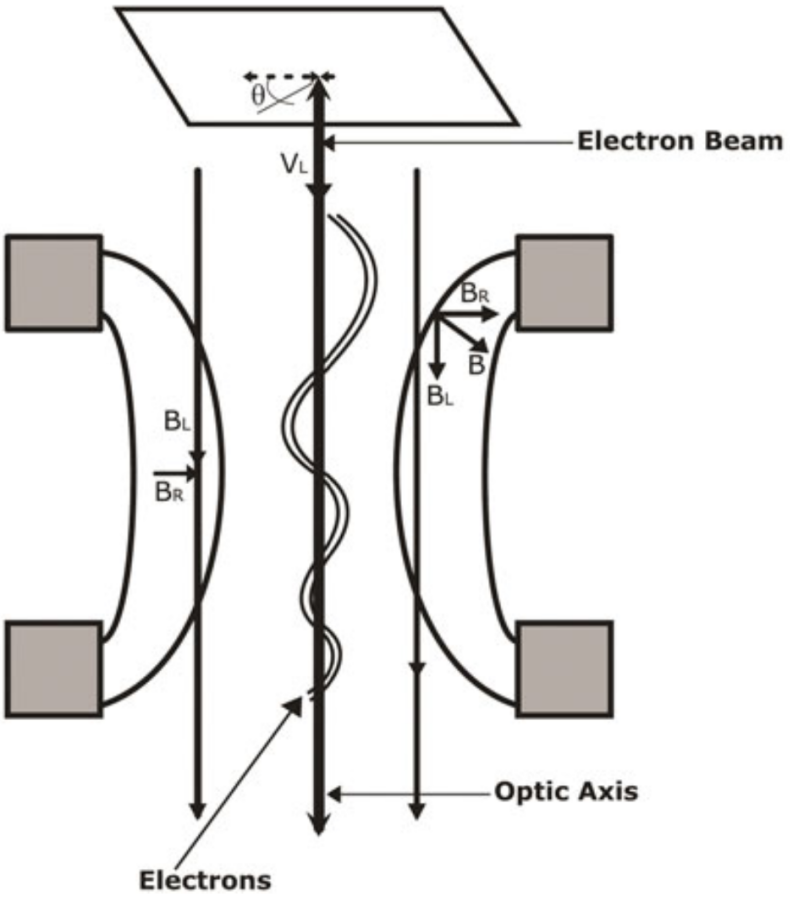

Figure 6: *Working of an electromagnetic lens: The radial component of the magnetic field makes the off-axis electrons go down the optic axis in a spiral. [1]*

(a)).

Analogous to optical lenses, the demagnification is defined as correlation between the distance from object plane to the center of the lens (p in Figure 8) and the distance from the center of the lens to the image plane (q in Figure 7) as follows

$$\text{Demagnification} = \frac{p}{q}. \tag{2.3}$$

The original object is the diameter d_0 while d_1, which is formed after the condenser lens, is considered its image. As seen in the Figure 7, d_1 is reduced in size compared to d_0 because of demagnification and also rotated. For the final lens, d_1 becomes the object and d_2 is its image and there is a further reduction in size of the probe d_1. Selection of a small spot size reduces image brightness but makes possible the formation of fine probe size that improves image resolution.

Inside the column there are thin rectangular pieces of molybdenum or 95% platinum - 5% iridium alloy called an aperture strip. It has precisely drilled central holes, termed **apertures**,

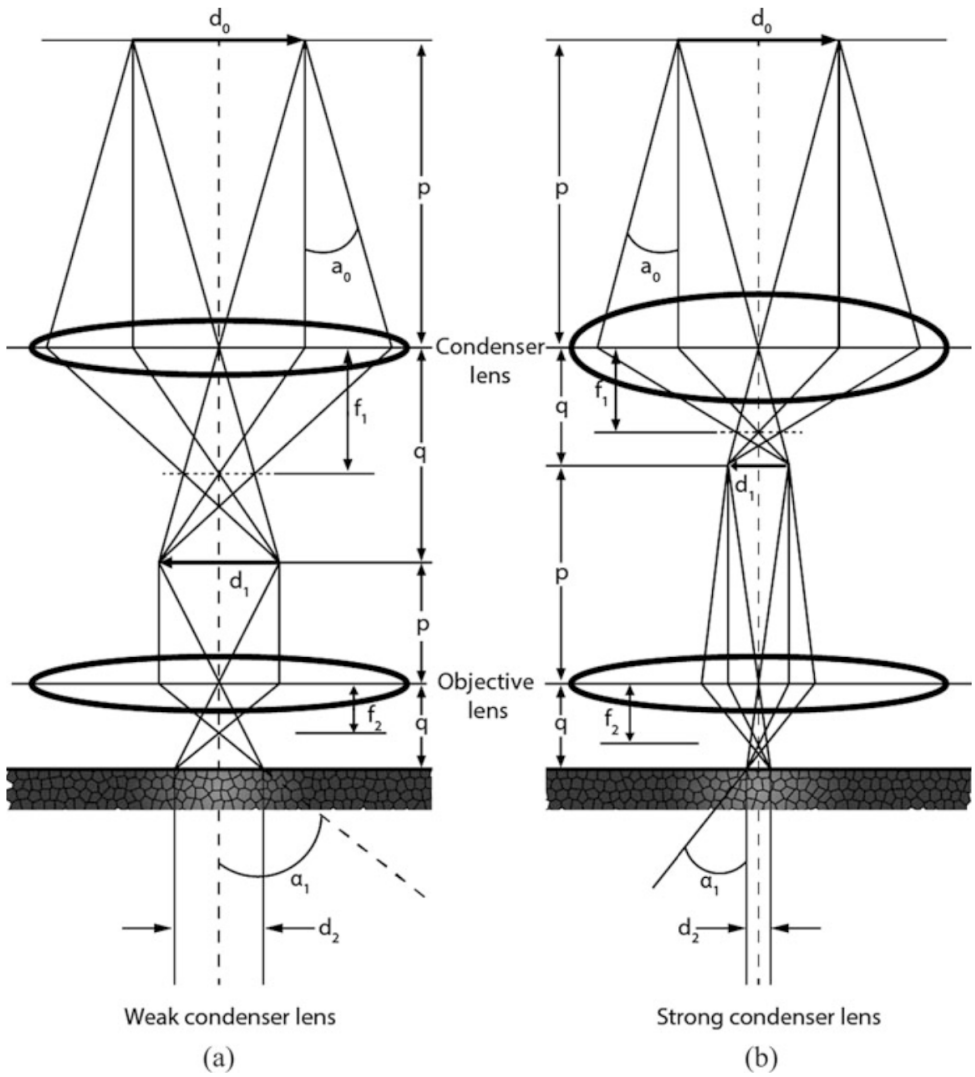

Figure 7: *A schematic diagram illustrates the application of lenses for demagnifying the electron beam. The initial lens is the condenser lens, followed by the objective lens. (a) Weak condenser lens results in large probe size, i.e., demagnification= $\frac{p}{q}$ is small. (b) Strong condenser lens results in small spot size, i.e., demagnification= $\frac{p}{q}$ is large. [1]*

to allow the beam to pass through. The radii of these aperture range from 10 μm to 500 μm. Apertures play a crucial role in regulating both the quantity and the convergence angle of electrons traversing the column, while also preventing off-axis electrons from reaching the specimen surface. This function helps mitigate the impact of lens defects, consequently enhancing image resolution. A smaller aperture leads to a reduced probe size with lower current, contributing to improved image resolution but a decrease in signal strength.

The final lens in the column is called the **objective lens** and it is designated as the probe forming lens in the SEM. The current in the objective lens is adjusted to demagnify and focus the electron beam on the surface of the specimen and it is controlled by the "*focus*" knob during the SEM operation.

Lens aberrations represent imperfections that restrict the electromagnetic lenses' capacity to

focus the beam into a precise and symmetrical probe. **Spherical aberration** arises due to the varying strength of the electromagnetic field near the lens's edge and the weaker field near the optic axis. Consequently, electrons near the edge experience stronger bending, leading to different focal points for the electron beam based on the lens section traversed. This divergence results in a disc formation rather than a point at the image plane, causing image blurring. To control spherical aberration, a small aperture is introduced after the objective lens. This aperture blocks off-axis electrons, preventing their contribution to image formation, and reduces the beam convergence angle. The outcome is a diminished beam diameter, limiting the number of electrons reaching the specimen and reducing brightness.

In electron beams at a given accelerating voltage, electrons do not share the same energy. Electrons with lower energy are strongly focused and cross the optic axis closer to the lens, while higher-energy electrons focus farther from the lens. This discrepancy gives rise to **chromatic aberration**, where different focal points cause electrons to converge in a disc shape instead of a point at the image plane. Chromatic aberration increases the probe size and diminishes image contrast. However, adjusting the accelerating voltage of the electron beam can eliminate this effect.

Minor flaws in lens construction, disparities in copper windings, or the presence of contaminants in apertures can lead to the lens generating an inconsistent electromagnetic field. In the case of **astigmatism**, two perpendicular line foci are formed at distinct focal lengths, causing the image to stretch in one direction on one side of the focus and perpendicular to it on the other side. Astigmatism induces a distortion in the probe's shape, transitioning from round to elliptical as the focus changes. Detection of astigmatism involves intentionally under-focusing and over-focusing the beam. If the image elongates in one direction during under-focusing and perpendicular to it during over-focusing, it unequivocally signals the presence of this defect. Although the stretching effect is eliminated at the precise focus, the image remains blurred because the probe diameter, under astigmatic conditions, exceeds the optimal size. Correction of astigmatism employs a stigmator, comprising an electromagnetic octupole lens situated near the pole pieces' gap within the objective lens. This coil applies an electromagnetic field with an appropriate strength at a 90-degree angle relative to the field distortion to counteract existing astigmatism. The goal is to restore the probe to a circular shape of minimal dimensions.

The surface of the specimen is systematically scanned by the electron beam, moving from left to right and point by point. A detector processes the signal generated at each discrete location on the specimen, synchronously presenting it on a corresponding pixel of the viewing monitor. This scanning action is facilitated by two sets of electromagnetic coils for deflection, positioned within the bore of the objective lens assembly in the electron column (**scanning coils**) (Figure 8).

These coils are linked to a scan generator, responsible for creating the raster pattern on the

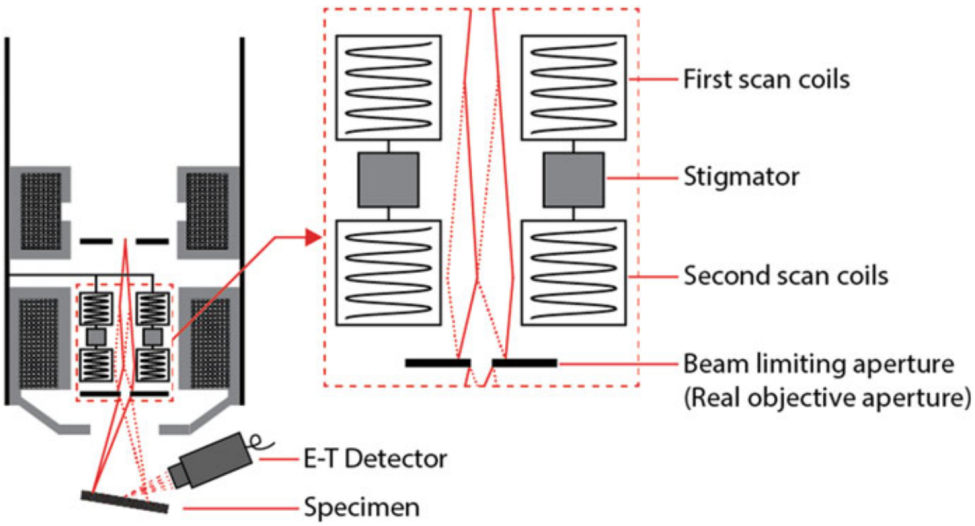

Figure 8: *A schematic diagram showing how scan coils work to create a raster on the specimen surface. [1]*

specimen. The beam traverses the region of interest on the specimen in a left-to-right motion (x-direction) and then returns to the starting point. It subsequently moves down a line (y-direction), rescanning from left to right, completing a comprehensive two-dimensional rectangular raster of the specified area. After completing the scan of the chosen area, the beam returns to the initial scan position to commence scanning for another image frame. The current in the coils is modulated over time to generate the raster. The first pair of coils deflects the beam away from the optic axis, and the second set of coils, located at the pivot point of the raster, brings the beam back to the axis. The number of lines in the image can vary from 500 to 2,000 depending on the ratio of frame and line scan frequencies. [1]

2.1.3 Specimen chamber

The specimen chamber, situated at the electron column's base, comprises a pre-chamber (Figure 9) and the main chamber, separated by a valve. The main chamber is consistently maintained under vacuum, while the pre-chamber can be vented for specimen replacement. After swapping the specimen, the pre-chamber is sealed and evacuated using a rotary vane vacuum pump. Once sufficient vacuum is attained, the valve is removed, enabling the specimen's placement in the main chamber. The main chamber requires a high vacuum (at least 10^{-3} Pa) to prevent electron beam-particle collisions, and it features a camera for specimen inspection. However, the camera must be turned off when the electron beam is active to avoid signal interference. Modern SEMs feature an infrared camera within the specimen chamber, displaying a live image on the computer monitor. This tool allows real-time monitoring of the specimen stage and holder movement, ensuring a safe distance from the objective lens pole piece to prevent collisions during microscopy at small working distances. The chamber is illuminated by infrared (IR)

light-emitting diodes (LED). While the backscattered detector is sensitive to IR rays, the EDS detector can produce false peaks or increased background in the spectrum when IR LEDs are active. Therefore, the IR camera and LEDs are turned off when these detectors are in use. [1]

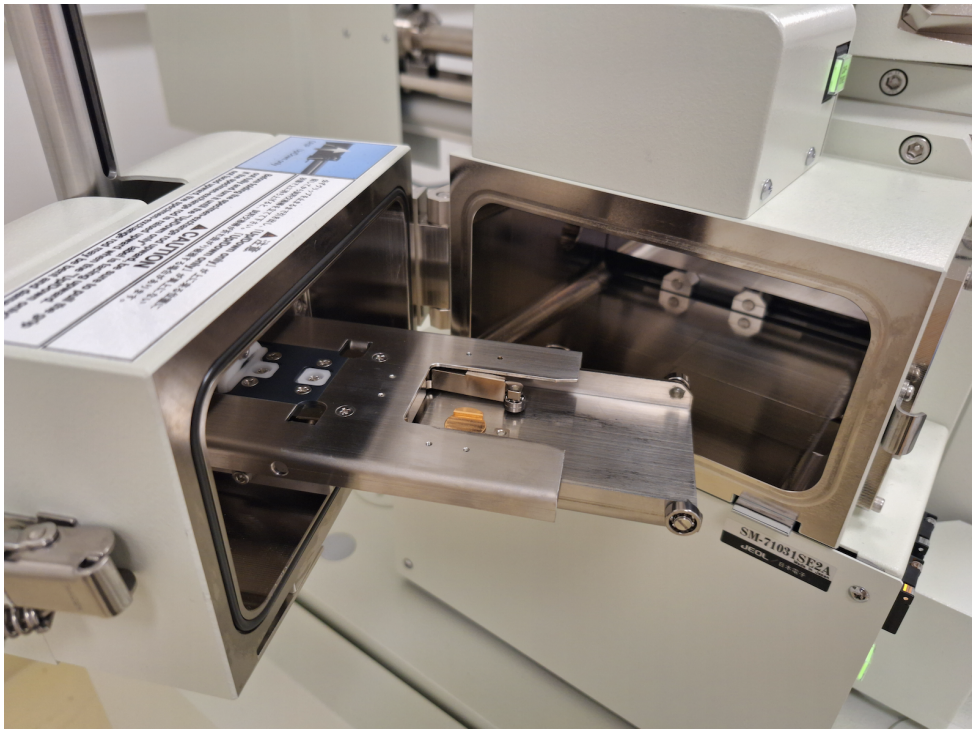

Figure 9: *Pre-chamber of the JEOL JSM-7610FPlus.*

2.1.4 Detectors

The detector in the SEM collects and converts signals from the specimen into electrical pulses, processed by SEM electronics to create an SEM image or an energy dispersive X-ray (EDS) spectrum. Vital for imaging and microanalysis, these detectors are installed in the specimen chamber. Some are permanent, while others can be mounted or dismounted as needed, and some are retractable. Their common function is to gather and analyze signals, including secondary and backscattered electrons for imaging and X-rays for specimen composition analysis. [1] Information that can be obtained from the specimen is depicted in Figure 10. Main detectors are Everhart-Thornley (E-T) detector and backscattered electron (BSE) detector.

The Everhart-Thornley (E-T) detector is designed to detect both secondary and backscattered electrons emitted by the specimen for imaging purposes. While it can capture backscattered electrons, its predominant application is in generating secondary electron images of the specimen surface. Due to its high efficiency in collecting secondary electrons and its pivotal role in SEM image formation, the E-T detector stands out as the most commonly utilized component in the microscope. **Secondary electrons** are a result of the inelastic scattering of the electron beam in a scanning electron microscope (SEM). When the high-energy electron beam interacts with the specimen's surface, valence electrons are ejected

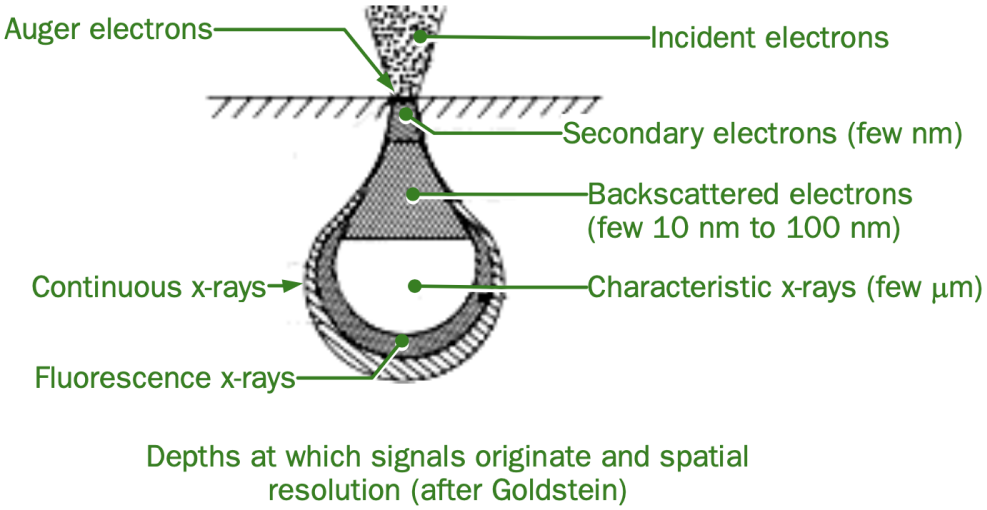

Figure 10: *Schematic depiction of depths at which signals originate and spatial resolution. [2]*

from the atoms in the material. These secondary electrons have lower energy than the incident electrons and can be harnessed for analyzing the topography of the sample since they come from a shallower sample depth.

The Everhart-Thornley detector is placed inside the specimen chamber close to the specimen which is located directly below the objective pole piece. The design of the Everhart-Thornley (E-T) detector features a tubular structure positioned at an angle of approximately 30 degrees to the specimen surface. To facilitate the collection of low-energy secondary electrons (0–50 eV) emitted from the specimen, a positive bias (+200–300 V) is applied to a wire mesh or collector grid, known as the Faraday cage, covering the detector's face (refer to the schematic in Figure 11).

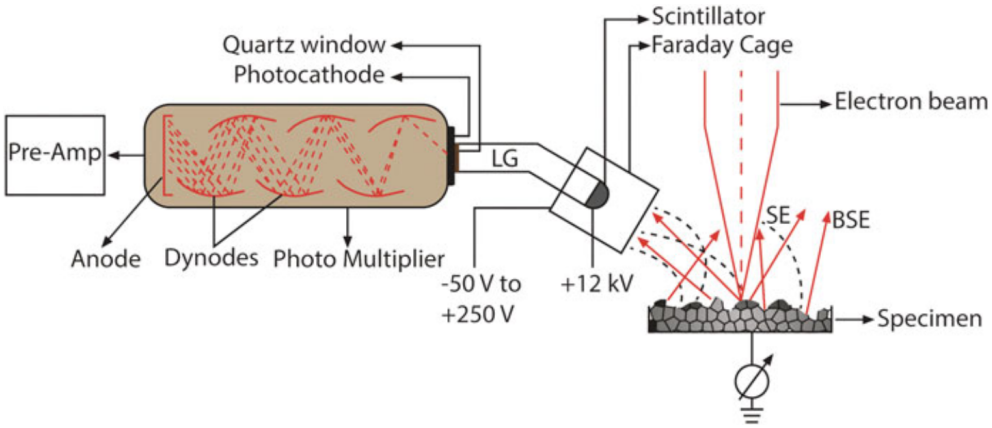

Figure 11: *Schematic showing the working of an E-T detector. SE, secondary electrons (0–10 eV); BSE backscattered electrons (10–30 keV); LG, light guide. Depicted are also Faraday cage, pre-amp and preamplifier component. [1]*

The Faraday cage plays a crucial role by not only directing secondary electrons toward the

detector but also enhancing the collection efficiency, especially for those with initial trajectories directed away from the detector. Additionally, tilting the sample towards the detector can be employed as a strategy to further optimize the collection of the secondary electron signal. The electrons, captured by the Faraday cage, impact the surface of the phosphorescent (cathodoluminescent) scintillator within the detector. However, the energy of these secondary electrons is insufficient, measuring only a few electron volts (eV), to generate a meaningful output from the scintillator. Measuring 8–20 mm in diameter, the scintillator surface is coated with a thin layer of metal, carrying a positive bias of +10–12 kV. This bias accelerates the incoming electrons towards the scintillator. Notably, the scintillator material possesses a high refractive index, strategically concentrating the electrons towards the light guide for further processing. The Faraday cage is insulated from the scintillator bias, providing protection against undesired deflection and distortion of the electron beam caused by the substantial potential on the scintillator surface. The bias applied to the Faraday cage is of negligible magnitude, ensuring minimal impact on the electron beam. As the charged electrons collide with the scintillator surface, they undergo conversion into a burst of visible light, known as photons or scintilla. The quantity of generated photons is dependent upon the kinetic energy of the incoming secondary electrons.

The generated light is then directed through a light guide, typically made of total reflection plastic or glass. This light, produced by the conversion of electrons, travels through a quartz window, which acts as a barrier between the light guide within the evacuated specimen chamber and the photomultiplier tube (PMT) positioned outside the SEM chamber. The quartz window serves the dual purpose of maintaining the vacuum within the specimen chamber while permitting the passage of light to reach the PMT. This combination of electron-to-light conversion (scintillation) and the quartz barrier facilitates the transmission of the signal from inside to outside the SEM chamber. The PMT itself is a sealed, evacuated glass container. The light strikes the thin layer of photocathode positioned at the forefront of the photomultiplier tube (PMT). This photocathode material, characterized by a low work function, releases electrons from its conduction or valence atomic shells upon light exposure. These low-energy electrons, known as photoelectrons, enter the PMT. Consequently, the PMT transforms light into electrons, directing them through a series of dynode electrodes, typically numbering eight. The initial dynode bears a positive bias (100–200 V) relative to the photocathode, propelling the photoelectrons toward this electrode. Upon striking the first dynode, secondary electrons are emitted. Subsequent dynodes maintain positive biases, facilitating the acceleration of secondary electrons and the creation of additional secondary electrons upon impact. This cascading effect leads to electron multiplication, resulting in a significant amplification of the electric signal. Signal gain reaches up to $\times 10^6$–10^8 without a notable increase in noise.

The electric signal at the output of the photomultiplier is further amplified by preamplifier (Pre-Amp) device that forms part of the E-T detector. The electric signal at the output of the

photomultiplier is further amplified by preamplifier (Pre-Amp) device that forms part of the E-T detector. Following its passage through the E-T detector, the signal undergoes amplification in an amplifier, elevating its strength to a level suitable for image creation on a computer monitor. However, before reaching the monitor, the signal traverses the video control unit and an image processing board for analog-to-digital conversion. The amplification process involving the PMT, preamplifier, and amplifier is crucial, given the initially minute current (i.e., quantity) of low-energy secondary electrons.

Backscattered electrons result from elastic scattering of electron beam upon the specimen surface and this is why their energy (several keV, depending on the accelerating voltage) can be significantly higher than that of secondary electrons (≈10 eV). This is why, because of the large difference in energy, the Everhart-Thornley detector can collect only backscattered electrons. However, it is more common to use separate fixed **backscattered electron detector (BSE)** and position it directly below the pole piece and above the specimen.

The most commonly employed backscattered detector is a solid-state diode (SSD) detector consisting of two electrodes making up p-n junction. High-energy backscattered electrons emanating from the specimen enter the backscattered detector attached to the end of the objective pole piece directly above the specimen (Figure 12) and are scattered inelastically within the semiconductor material. The front end of the detector features a gold electrical contact (approximately 10–20 nm thick), coated onto a thin layer of Si (referred to as the "dead layer"), followed by a Si semiconductor layer with a thickness of a few tenths of a micron. Gold contacts are applied to both surfaces of the detector for the application of bias voltage. [1]

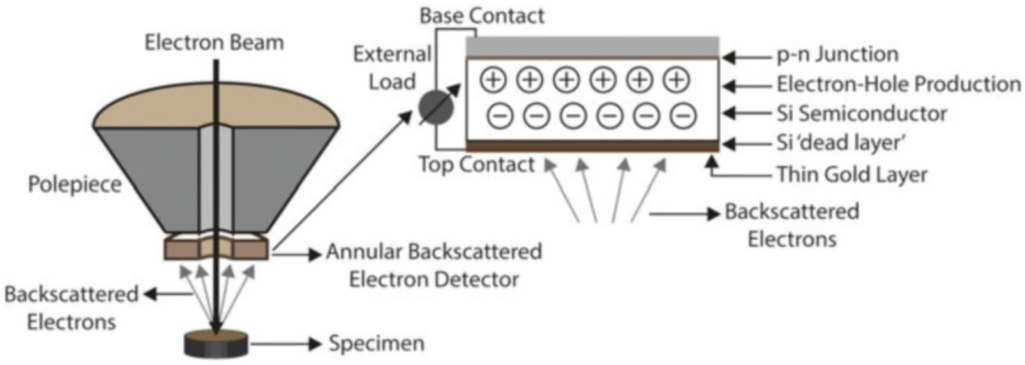

Figure 12: *The backscattered detector is affixed to the lower extremity of the pole piece, directly positioned above the specimen. The design of the backscattered electron (BSE) detector is depicted in a schematic located at the upper right-hand side. When backscattered electrons collide with the surface of the solid-state semiconductor detector, they generate electron-hole pairs. [1]*

Backscattered electrons (BSE) from the specimen undergo inelastic scattering interactions with the electrons in the Si lattice, causing the movement of electrons from valence to the conduction band of Si, leaving behind a hole and creating an electron-hole pair. The resulting current in the detector is directly proportional to the number and energy of backscattered

electrons interacting with it. The more numerous and energetic the BSE striking the detector surface, the greater the number of electron-hole pairs produced. To prevent recombination, an electric field is applied before the electrons can return to their vacated spaces. In semiconductor devices, the p-n junction serves this purpose, creating an internal field to keep electrons and holes separated, allowing current to flow in a single direction. The amplified current is then used to generate a signal with sufficient strength to produce an image. The detector's sensitivity to the quantity and energy of electrons from the specimen contributes to the observed contrast in the backscattered image. [1]

2.2 Imaging with the SEM

The scanning electron microscope is commonly employed for the characterization of diverse materials owing to its user-friendly operation, straightforward sample preparation, and easy image interpretation. Novice users can quickly acquire images with minimal practice. Nonetheless, achieving high-resolution microscopy and analyzing "challenging" samples necessitate experience and a grasp of the principles governing image formation in the SEM.

Influence of operational parameters on SEM images

The scanning electron microscope stands as a powerful instrument for capturing detailed microstructural features of materials. Basic microscopy at low magnification and imaging of conductive samples are relatively uncomplicated tasks. Yet, achieving high-resolution microscopy demands a comprehension of optimal imaging conditions and operational parameters to generate top-notch images that unveil intricate surface structures. Additionally, possessing the necessary know-how aids users in interpreting SEM images and discerning and distinguishing between factors that influence the results. The subsequent sections provide explanation of some of the crucial imaging parameters.

2.2.1 Effect of accelerating voltage (beam energy)

The accelerating voltage, defined as the potential difference between the filament and the anode, significantly influences various aspects of microscopy. It directly impacts the resolution of surface features, spatial resolution, brightness, chromatic aberration, interaction volume, edge effect, charge buildup, beam contamination, and, if applied, the strength of analytical X-ray signals. Higher accelerating voltages result in a smaller electron probe diameter, enhancing spatial resolution and brightness. They also mitigate the adverse effects of chromatic aberration. However, excessive beam energy can lead to increased beam penetration, generating larger excitation volumes and low-resolution signals, like backscattered electrons, diminishing image contrast and concealing fine surface features.

Conversely, operating the SEM at lower accelerating voltages, around 5 kV, confines

specimen-beam interaction close to the surface, yielding images rich in surface detail. This approach is fundamental to low-voltage microscopy, especially in field emission scanning electron microscopes, facilitating high-resolution imaging. Lower accelerating voltages are particularly suitable for examining fragile or soft samples (such as cells and polymers), as well as features present in low quantities, revealing fine surface structures due to limited electron beam penetration into the sample.

2.2.2 Effect of probe current/spot size

The current responsible for striking the specimen and inducing various signals is termed the probe current. For a given beam energy, a smaller current yields a correspondingly smaller probe size. The spatial resolution of a scanning electron microscope is primarily contingent on the probe size of the incident beam. Achieving a smaller electron probe diameter corresponds to higher image resolution in the SEM with less risk of beam damage, although excessively low probe currents may result in grainy images that obscure surface details. Higher probe currents yield smoother images but compromise image resolution and may induce beam damage. [1]

2.2.3 Effect of working distance

The working distance (WD) denotes the distance between the pole piece of the objective lens and the plane of optimum focus. Adjustment of the working distance is accomplished by moving the sample stage along the z-axis and focusing the beam on the sample surface, while maintaining a constant objective lens current. Proximity to the lens enhances image resolution but diminishes the depth of field. Large WD increases the depth of field due to a smaller convergence angle and this configuration enables the observation of specimens at low magnifications. However, a large WD compromises spatial resolution due to an increased probe diameter. [1]

2.2.4 Effect of specimen tilt

At times, the specimen is deliberately tilted at specific angles to accentuate features that might not be easily discernible otherwise. This tilting technique is employed to highlight surface topography, provide side or cross-sectional views, and capture stereo micrographs that convey a 3-D visual impression. However, it's crucial to note that displayed magnifications lose validity during tilt and must either be corrected or obtained at zero tilt angles when the sample lies flat perpendicular to the beam. Tilting the specimen can introduce distortion in the image due to the extended path the beam scans across the specimen during tilt, projecting it onto the same length of scan. [1]

2.2.5 Column modes

There are standard modes in scanning electron microscopy such as Secondary Electron Mode (SEM) and Low Vacuum Mode (LM) (however, there are microscopes specially designed to work exclusively in Low Vacuum Mode). In the SEM mode, scanning electron microscope primarily detects secondary electrons emitted from the sample surface due to the interaction with the primary electron beam. It provides high-resolution images of the sample's surface topography. Low Vacuum Mode allows SEM imaging at reduced chamber pressure, which is particularly useful for non-conductive or hydrated samples. It helps to minimize charging effects and allows imaging without coating non-conductive samples. [1]

The manufacturer, *JEOL*, of the scanning electron microscope that was used in our research has trademarked the Gentlebeam mode. During SEM specimen observation, specimen charging is a prominent imaging artifact that can lead to various distortions, including image flattening, high or low contrast, and overall distortion. To mitigate this effect, two primary strategies are commonly employed: applying a conductive coating to the sample or reducing the primary beam voltage. Modern SEMs offer the capability to achieve nanometer-sized spot sizes even at 1kV and below, enabling high-resolution imaging and analysis of nanomaterials and surfaces without the need for conductive coatings. To enhance SEM performance at low voltages, JEOL has implemented a beam deceleration function known as Gentle Beam, as illustrated in Figure 13. [3]

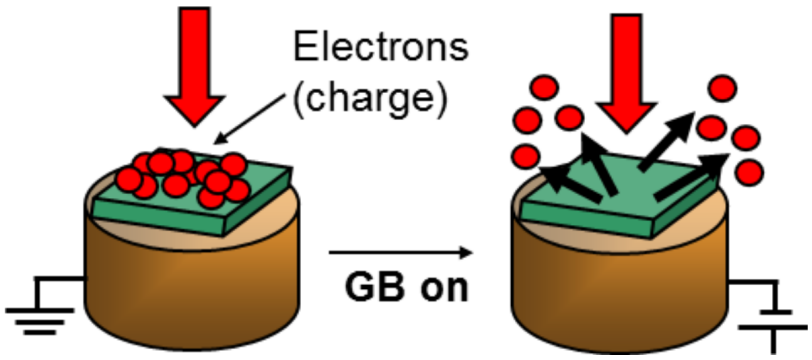

Figure 13: *Gentle Beam principle. [3]*

Gentle Beam operates by slowing down the primary beam voltage through a negatively charged stage bias, resulting in a lower landing energy. This not only aids in charge balance but also effectively reduces lens aberrations, thereby enhancing overall image resolution. The landing voltage ($E_{\text{landing}} = E_{\text{gun}} - E_{\text{bias}}$) can be adjusted by combining the electron source voltage and specimen bias, allowing for optimal charge balance and high-resolution performance at ultra-low voltages. Specimen bias typically ranges from 0-2 kV, with improved performance achievable at bias values up to 5 kV. [3]

Effects of electron beam on the specimen surface

2.2.6 Specimen charging

The primary beam current (i_B) entering the specimen equals the sum of the specimen current (i_{sp}) flowing out of the specimen into the ground and the currents of backscattered and secondary electrons (i_{BSE} and i_{SE}, respectively) ejected from the specimen, as illustrated in the following equation:

$$i_B = i_{sp} + i_{BSE} + i_{SE}. \tag{2.4}$$

Rearrangement of the above equation gives specimen current i_{sp} as:

$$i_{sp} = i_B - i_{BSE} - i_{SE} \tag{2.5}$$

or

$$i_{sp} = i_B - \eta - \delta \tag{2.6}$$

where η and δ are the BSE and SE yield, respectively, which is the ratio of the number of backscattered/secondary electrons emitted from the specimen to the number of incident primary electrons.

Throughout the scanning process, the beam current (i_B) remains constant, while the coefficients η and δ undergo variation. At typical accelerating voltages used for imaging (greater than 5 kV), the combined number of electrons leaving the specimen as secondary electrons (SE) and backscattered electrons (BSE) – referred to as the total electron coefficient (η + δ) – falls significantly short of the beam current entering the specimen (i_B). For instance, a pure copper (Cu) target imaged at 20 kV demonstrates a total electron coefficient of only 0.4. This indicates that 60% of the beam electrons entering the specimen must exit through electrical contacts to prevent accumulation within the specimen, necessitating grounding of the specimen stage. In the case of a conductive metal target like Cu, beam electrons traverse the specimen and specimen holder to reach the grounded specimen stage. A continuous conductive path from the specimen surface to the ground is essential for this purpose.

However, when scanning an uncoated insulating specimen, a conductive path for grounding the specimen current (i_{sp}) is absent. Electrons in the beam that strike the insulating specimen surface lack a conductive path to dissipate, leading to their accumulation within the specimen. This accumulation forms a localized negative charge known as charge buildup or specimen charging. Such electrostatic charging raises the local potential, disrupting normal secondary

electron emission and severely compromising the imaging capability of the SEM. This charging results in horizontal lines on images, beam shift, and image distortion.

There are a few methods to reduce charge build. To address charge buildup on nonconductive specimens, a common practice involves coating the surface with a thin conductive film like platinum, gold, carbon, tungsten, etc., prior to SEM examination. The coating, typically a few nanometers thick with small grain size, does not interfere with surface morphology examination at various magnifications. However, for ultrahigh-resolution imaging, special attention is required to ensure that the imaging captures the actual specimen features rather than the coating grains. Establishing electrical contact with the specimen holder and stage is achieved using conductive paint or tape.

Polymer specimens commonly experience significant charge buildup during microscopy. While coating with a conducting metal layer is generally necessary, it is crucial to minimize the coating thickness to avoid masking specimen features. This precaution is particularly crucial during low-voltage imaging, where beam penetration into the specimen is limited, potentially causing contrast due to the coated layer rather than the underlying specimen surface.

The second method of reducing the charge build is use of low accelerating voltage, beam deceleration and small probe current. To mitigate charge buildup, these techniques aim to reduce the influx of electrons entering the specimen.

Another technique for reducing charge buildup is proper specimen mounting. Carbon tape is commonly employed as a sample mounting material in SEM applications. While it enhances specimen conductivity, there is a potential drawback as carbon tape may undergo outgassing[1] in the SEM chamber, creating conditions favorable for charge buildup on the specimen. To manage these conflicting effects, it is advisable to use a minimal amount of tape and limit the duration of microscopy sessions. Moreover, for adequate conductivity, it is essential to secure the sample to the underlying tape using additional carbon or silver tape. [1]

Furthermore, as explained in section 2.2.4., altering the tilt of a specimen influences the yield of backscattered and secondary electrons. This phenomenon can be strategically utilized to mitigate the charging effect by tilting the specimen to an angle that promotes increased emission of electrons from the surface. Electron energy filters, including the *JEOL* patented r-filter, are employed to segregate electrons based on their energy, effectively diminishing the impact of low-energy secondary electrons and thereby mitigating charging effects.

The r-filter can be adjusted in the menu window and it has three modes which enables the choice of information on the topology or composition of the specimen that can be inferred from the sample. In SB mode (regarded as the standard mode) all detectable secondary and backscattered electrons are detected and the image has the largest signal-to-noise ratio. SE mode is used for detecting low energy secondary electrons by filtering out the backscattered electrons.

[1] Refers to the release or emission of gas or vapors from a material, in this case, carbon tape.

This enables observation of topographic images of the specimen surface. Mainly backscattered electrons are detected in BE mode and it is done by filtering low energy secondary electrons. The contrast in these images depends on differences in the composition. [2]

2.2.7 Surface contamination

Extended scanning of a specimen's surface can lead to image degradation, manifesting as a loss of sharpness and the emergence of a dark rectangular smudge. This smudge is a consequence of carbon deposition resulting from the interaction between the electron beam and residual gas molecules near the specimen surface. Typically, these residual gases consist of ionized volatile hydrocarbon molecules[2], depositing nonvolatile carbon on the scanned area—an occurrence referred to as specimen contamination. Zooming out during live imaging reveals this contaminant layer.

Despite the SEM specimen chamber being under vacuum, trace gas molecules persist. Potential sources of these contaminants include hydrocarbons introduced by the specimen's outgassing, organic materials used in specimen preparation, instrument surfaces or grease, and backpressure from the rotary oil pump evacuating the SEM chamber. Residual hydrocarbon molecules may also be present on SEM column components, such as apertures, leading to beam interaction and the formation of contaminants on these surfaces, potentially causing beam instability. Contamination becomes a critical concern, especially during imaging at very low accelerating voltages and probe currents when the electron beam lacks the energy to penetrate the deposited contaminant layer. In such cases, the contaminants might be imaged instead of the underlying specimen surface. [1]

2.2.8 Beam damage

During the interaction between the electron beam and the specimen, heat is generated due to ionization at the irradiated spot, where energy is transferred from the beam to the specimen. The level of temperature reached and the amount of heat generated depend on factors such as the accelerating voltage, probe current, exposure time, specimen area, and the specimen's ability to dissipate heat. The extent of damage varies based on the material of the specimen. Conductive materials like metals and alloys can effectively dissipate heat, making them more resistant to beam damage. In contrast, polymers and biological specimens, being poor conductors of heat, are more susceptible to beam damage. The manifestations of radiation damage include cracks, bubbles, holes, depressions, and dimensional changes.

[2]Ionized volatile hydrocarbon molecules refer to hydrocarbon compounds (molecules consisting of hydrogen and carbon) that have undergone ionization, a process in which one or more electrons are removed from the molecule, resulting in the formation of positively charged ions. In the context of SEM specimen contamination, "volatile" refers to the tendency of a substance to readily evaporate or turn into a gas under normal conditions. Volatile hydrocarbon molecules are those hydrocarbons that can easily vaporize into the surrounding environment.

To mitigate beam damage during the imaging of sensitive specimens, certain precautions can be taken, such as using a low accelerating voltage, reducing probe current, minimizing exposure time, employing low magnifications with larger scan areas, and applying conductive coatings like gold or platinum to the specimen surface to enhance thermal conductivity. [1]

3 Energy dispersive X-ray spectroscopy (EDS)

In many instances, is is desirable to extract chemical information from specimens undergoing SEM examination. This is typically achieved through the application of energy dispersive X-ray spectroscopy (EDS). The SEM column is equipped with an EDS detector, allowing for the detailed examination of localized chemistry within a specimen. This integrated system not only identifies the elements that make up a phase (qualitative analysis) but also quantifies their concentrations (quantitative analysis). The efficiency and nondestructive nature of microchemical analysis contribute significantly to materials verification and phase identification.

During the interaction of the primary electron beam with the specimen, characteristic X-rays and white radiation (background X-rays), collectively forming an X-ray signal, are generated. An X-ray detector is employed to collect this signal, measure its energy and intensity distribution, and analyze it for the identification of elements and determination of their concentrations within the analyzed region of the specimen material.

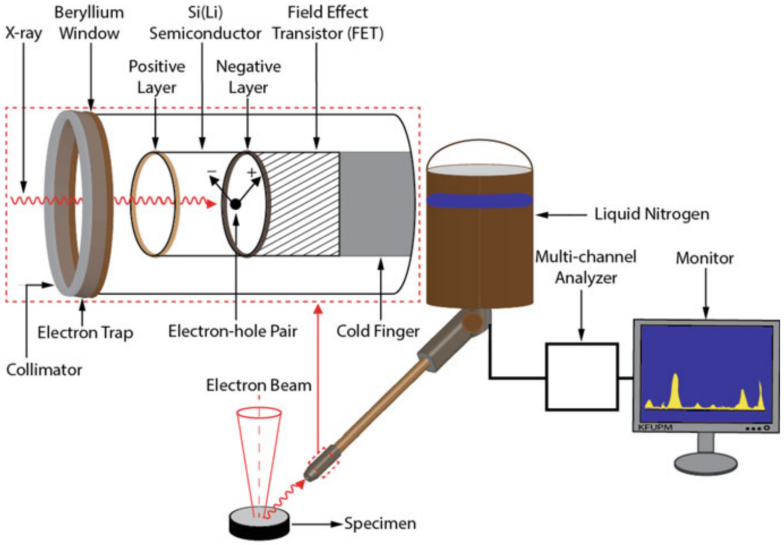

Figure 14: *A schematic diagram of the EDS detector setup commonly used in the SEM. In our research cooling was done using a thermoelectric cooler. [1]*

Figure 14 displays a schematic diagram of the EDS detector setup commonly used in the SEM. A collimator tube, situated at the front end of the detector, restricts the collection to X-rays originating solely from the specimen, preventing stray X-rays or backscattered electrons from entering the detector. After passing through an electron trap, a thin opaque window isolates the SEM chamber environment from the detector. The window is succeeded by a semiconductor crystal, usually made of silicon or germanium, which is sensitive to light. The ultrathin window, often polymer-covered with an evaporated aluminium layer and supported with a silicon grid, acts as a shield to protect the crystal and maintain a vacuum within the detector assembly. X-rays emitted from the specimen pass through the thin window and reach the semiconductor

diode detector, where they ionize Si atoms through the photoelectric effect, generating electron-hole pairs. The resulting charge pulses, proportional to the number of electron-hole pairs created, are counted, and the energy of the X-ray photons responsible for the pulse output is calculated[3]. The automated system produces an output in the form of a labeled X-ray spectrum. It's worth noting that the first three elements of the periodic table (H, He, and Li) are not detected due to their inability to produce characteristic X-rays. [1]

[3]The standard energy required to create a single electron-hole pair in undoped silicon (Si) is established at 3.86 electron volts (eV). The detector tallies the count of charge pulses, and by multiplying this count by 3.86, the energy of the corresponding X-ray photons is calculated. For instance, with a count of 1642 pulses, the derived X-ray energy is 1,659 × 3.86, resulting in 6,403 eV or 6.4 kilo-electron volts (keV). This energy is associated with the K_α X-ray line, emitted when an electron undergoes a transition from the L to K (innermost) shell in the iron (Fe) atom. The consistent energy value for this transition facilitates the identification of iron as a potential constituent in the examined specimen, particularly when a pulse count of 1,659 is recorded. The higher the frequency of this specific pulse count, the greater the concentration of iron within the material.

4 Magnetron sputtering

As previously stated, due to their non-conductive nature, polymers often manifest issues related to charging when exposed to electron beams, leading to undesirable effects such as poor signal output, bright spots, image shift, and the appearance of snowy images. To mitigate these challenges, polymers are commonly coated with a thin layer of metal.

Various methods exist for applying coatings in a vacuum environment through physical vapor deposition, which can be broadly categorized into two main groups: (i) those employing thermal evaporation techniques, where the material is heated in a vacuum until its vapor pressure exceeds the ambient pressure, and (ii) those utilizing ionic sputtering methods, where high-energy ions collide with a solid, dislodging atoms from its surface. Ionic sputtering techniques include diode sputtering, ion-beam sputtering, and magnetron sputtering. Magnetron sputtering is a high-rate vacuum coating method used to deposit metals, alloys, and compounds onto various materials with thicknesses of up to about 5 μm. It offers advantages over other vacuum coating methods, leading to applications in microelectronics, decorative coatings, and more.

Sputtering involves ejecting atoms or molecules from a target material by bombarding it with high-energy particles. To make sputtering a practical coating process, specific conditions must be met. Firstly, ions with sufficient energy must be generated and directed toward the target's surface to dislodge atoms. Secondly, the ejected atoms must have the freedom to move toward the object to be coated, necessitating a vacuum environment to maintain high ion energies and minimize atom-gas collisions post-ejection. [4]

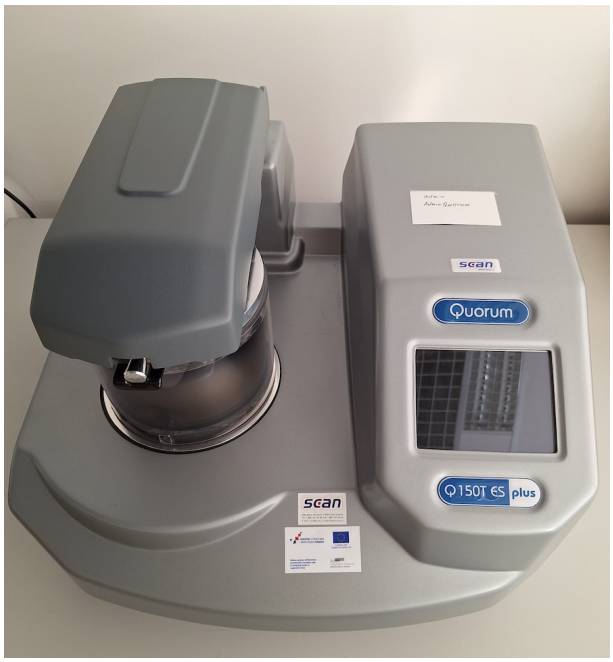

Figure 15: *Sputter coater used in our research.*

Modern coaters (Figure 15) for magnetron sputtering typically involve a vacuum chamber

where the sputtering process takes place. The chamber is evacuated to create a vacuum, reducing the number of gas molecules and preventing interference with the sputtering process. An inert gas (commonly argon) is introduced into the chamber. This gas will be used to create the plasma. The cathode (often the target material for deposition) and anode are arranged in the chamber. The cathode is typically negatively biased. A power supply is used to apply a high voltage to the cathode, creating an electric field. Electrons are emitted from the cathode and are then accelerated towards the anode. When the electrons possess sufficient energy, they ionize gas molecules, creating a plasma, leading to the appearance of a characteristic glow, indicative of energy-level transitions in the gas. In a magnetron sputtering system, magnets are often used for trapping primary and secondary electrons in a localized region close to the cathode to enhance ionization, leading to a more efficient plasma. The resulting positive gas ions move toward the cathode, causing ion impact on its surface. This ion impact generates secondary electrons and sputtered atoms, with the sputtering process involving the ejection of atoms from the cathode surface. The sputtered atoms are then deposited onto a substrate to create a thin film coating. Magnetron sputtering, with its racetrack-like electron paths, often provides better film uniformity and coverage of complex shapes compared to traditional sputtering methods. [4]

5 Atomic force microscopy

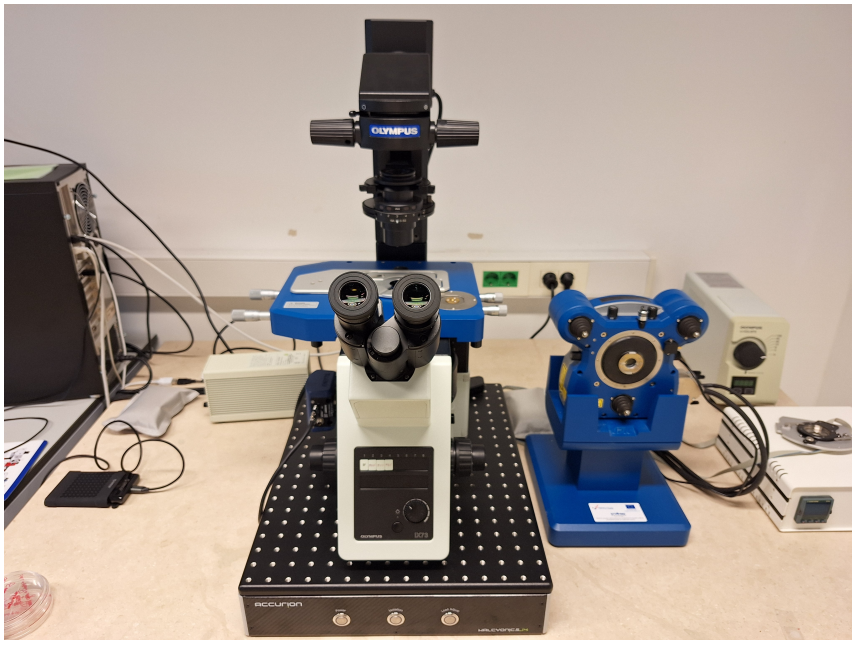

Figure 16: *AFM used in our research.*

Atomic force microscopy (AFM) (Figure 16) is a remarkable technique that offers high resolution and accuracy for observing and measuring surface structures. With an AFM, one can capture images revealing the arrangement of individual atoms or the structure of molecules with exceptional detail. One of its key advantages is its versatility, allowing the imaging in different ambient conditions, from hard surfaces like ceramics to dispersions of metallic nanoparticles, as well as soft materials such as flexible polymers, human cells, or individual DNA molecules. Unlike optical or electron microscopes, AFM doesn't rely on focusing light or electrons onto a surface. Instead, it physically 'feels' the sample's surface using a sharp probe. This probing creates height data, which, with simple data treatment, can be converted into images representing the sample's surface features. AFM holds the advantage of imaging samples without any prior treatment in an ambient atmosphere. This can reduce the introduction of artifacts associated with vacuum drying or the coating procedure. [5]

5.1 AFM instrumentation

The essential components of an AFM system consist of the microscope stage, control electronics, and a computer. Within the microscope stage, there is a scanner responsible for moving the AFM tip in relation to the sample, or vice versa, a sample holder, and a force sensor to monitor the tip. Additionally, the stage often integrates an optical microscope for visualizing the sample and tip. To enhance resolution and reduce noise, the stage is typically placed on a vibration isolation platform. The control electronics, usually housed in a sizable box, serve as the interface between the microscope stage and the computer. These electronics

generate signals to drive the scanner and other motorized elements in the microscope stage. They also digitize signals from the AFM for display and recording on the computer. [5]

5.1.1 Piezoelectric scanners, force transducers and feedback control

To understand the functioning of an AFM, it is essential to grasp three fundamental concepts: piezoelectric transducers[4], commonly referred to as piezoelectric scanners, force transducers and feedback control. In essence, the piezoelectric transducer facilitates the movement of the tip across the sample surface, the force transducer detects the force between the tip and the surface, and the feedback control loop channels the signal from the force transducer back into the piezoelectric system to uphold a constant force between the tip and the sample in the most simple mode of operation.

Piezoelectric materials function as electromechanical transducers, converting electrical potential into mechanical motion[5]. These materials can occur naturally and exhibit crystalline, amorphous, or polymeric structures, although synthetic ceramic materials are commonly employed in AFM applications. When an electric potential is applied across two opposite sides of a piezoelectric device, it undergoes a change in geometry. The extent of this dimensional change is influenced by factors such as the material properties, device geometry, and the applied voltage magnitude[6]. The precise control of these minute movements is what renders piezoelectric materials highly valuable in AFM.

The force between an AFM probe and a surface is measured using a force transducer. As depicted in Figure 17, as the probe makes contact with the surface, the voltage output from the transducer rises. Typically, the force transducer in an AFM comprises a cantilever with an integrated tip (serving as the probe) and an optical lever.

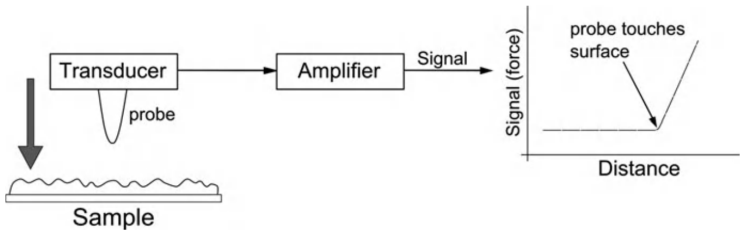

Figure 17: *Scheme of force transducer operation. [5]*

As depicted in Figure 18, the control electronics utilize the signal from the force transducers to drive the piezoelectrics, ensuring the maintenance of the probe–sample distance and, consequently, the interaction force at a set level. In case the probe detects an increase in force, the feedback control prompts the piezoelectrics to move the probe away from the surface.

[4]Transducers are devices or instruments that convert one form of energy into another.

[6]In other applications, they may also be used in the opposite sense, for example, if a change is caused in the material's dimensions they will generate an electrical potential.

[6]Usually, a single piezoelectric device exhibits an expansion coefficient of around 0.1 nm per applied volt.

Conversely, if the force transducer notes a reduction in force, the probe is shifted towards the surface.

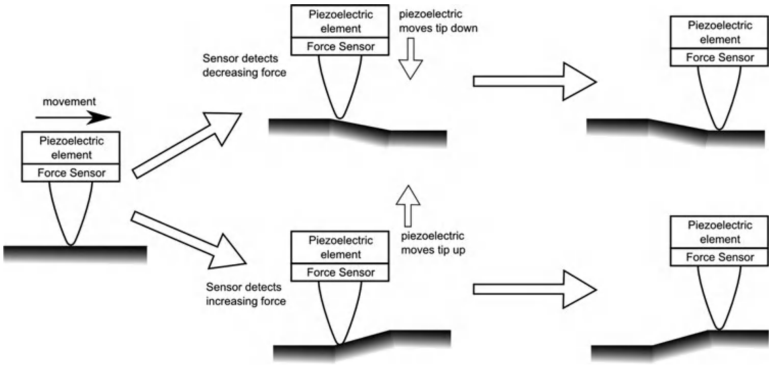

Figure 18: *Schematic of feedback control. [5]*

The typical design of an AFM is depicted in Figure 19. The x-y piezoelectric elements are used to scan the probe in a raster-like pattern across the surface. The movement of the z piezoelectric, adjusting up and down to uphold the fixed tip-sample distance, is presumed to be proportional to the sample topography. Thus, by monitoring the voltage applied to the z piezo, a height image, representing the surface shape, can be obtained. [5]

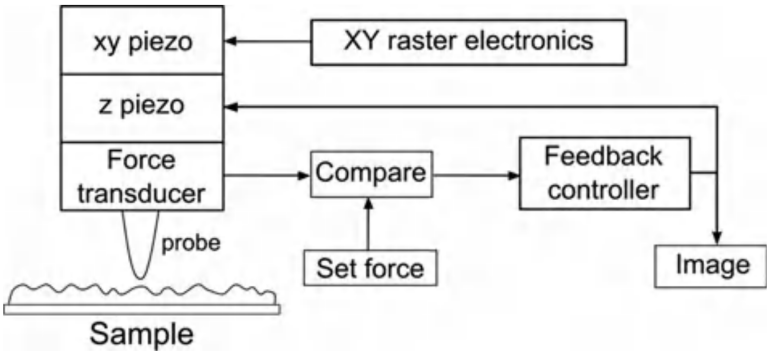

Figure 19: *Block diagram of AFM operation. [5]*

5.1.2 The AFM stage

The main part of the instrument is the AFM stage and it comprises of coarse approach mechanism, the Z motor (which moves the AFM scanner to the sample), coarse X-Y positioning stage, fine movement x-y-z scanners (piezos), force sensors and optical microscope.

Electronically, piezos function as capacitors, storing charges on their surface. Once charged, the piezoceramic retains its charge until dissipated. All piezoceramics exhibit a natural resonance frequency determined by their size and shape. Below the resonance frequency, the ceramic follows an oscillating frequency, experiencing a 90° phase change at resonance and a 180° phase change above resonance. [5]

The force sensor in an AFM must be capable of measuring extremely low forces, as a sharp probe necessitates a low applied force to avoid probe breakage due to high pressure (force/area). Currently, the majority of AFMs utilize optical lever force sensors. The design of an optical lever AFM sensor is depicted in Figure 20.

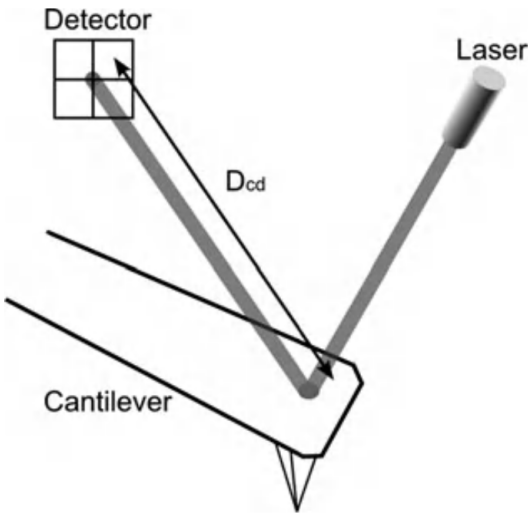

Figure 20: *Schematic diagram of the optical lever sensor. D_{cd} denotes detector distance. [5]*

A laser beam reflects off the back side of a reflective cantilever onto a four-segment photodetector. Interaction of the probe, mounted on the front side of the cantilever, with the surface alters the reflected light path. Force is then determined by monitoring the change in light detected by the four quadrants of the photodetector. Cantilevers are typically small, ranging from 50 to 300 microns in length, 20–60 microns in width, and 0.2 to 1 micron in thickness. The optical lever AFM force sensor requires alignment whenever the probe is changed. Typically, alignment is achieved by initially positioning the laser beam onto the cantilever and then verifying that the light is reflected onto the center of the photodetector by observing the photodetector signal. Shift of this signal indicates force exerted onto the cantilever.

The coarse X-Y positioning stage serves to align the sample with respect to the probe and it comprises of two screws — one for x-directional movement and the other for y-directional movement. Once the sample is appropriately positioned, the screws can be disengaged from the sample stage by rotating them in the opposite direction, minimizing vibrations and associated noise. The optical microscope, an optional component of the stage, facilitates locating the specific region on the sample intended for scanning. [5]

5.1.3 AFM cantilevers and probes

An optical lever-based AFM force sensor relies on a cantilever with a probe at its tip for functionality, where the probe's geometry significantly impacts the quality of AFM-measured

images. AFM cantilevers can theoretically be crafted from any material suitable for a spring-like structure. Silicon nitride (Si_3N_4) and silicon (Si) are the two commonly employed materials for AFM cantilevers. Cantilevers for optical lever-based AFM operate in two primary topography modes: contact (static) and oscillating mode. The resolution of a standard AFM is predominantly influenced by the shape and and aspect ratio of the probe tip, with sharper tips yielding superior resolution. The handling of AFM equipment demands carefulness as the probe tip is prone to damage, which can occur during probe mounting, tip approach to the specimen, or through contamination by the specimen. [5]

5.2 AFM modes

Atomic Force Microscopy operates in various modes to characterize different surface properties. The two primary modes are contact (static) mode and oscillating modes.

To comprehend the operational principles of various modes, it is essential to analyze a force-distance curve (Figure 21). When the probe is distant from the sample surface, it experiences no force, remaining straight, i.e. unbent. Upon reaching distance *b*, the probe encounters an attractive force that pulls it downward, causing the cantilever to bend. The highest attraction occurs at distance *a*, beyond which the force weakens until it becomes repulsive, leading to an upward bend in the cantilever. [5]

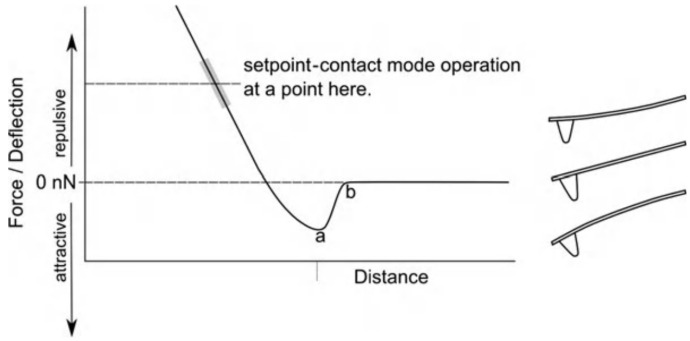

Figure 21: *Simplified force–distance curve showing contact scanning regime. Right: illustration of probe bending in each regime. [5]*

5.2.1 Contact mode (Static mode)

In this mode, the AFM tip maintains constant contact with the sample surface. As the cantilever scans (scratches) the surface it experiences changes in deflection. These deflection changes are used to maintain a constant force between the tip and the sample. Hooke's law expresses the force applied by the probe as $F = -k \cdot D$, where k represents the cantilever force constant, and D is the deflection distance. The deflection signal of the cantilever functions as the error signal, indicating the extent to which the height requires correction through piezoelectric adjustments.

Contact mode is suitable for imaging relatively flat and rigid samples. [5]

5.2.2 Oscillating mode^{TM} (Tapping Mode)

Tapping mode involves the oscillation of the cantilever at or near its resonance frequency, which is achieved with an additional piezoelectric element. When the probe encounters a force from the surface, the oscillation pattern is altered, leading to damping that diminishes both the frequency and amplitude of the oscillations. The force sensors monitor these oscillations, and upon detecting damping, the height is regulated through feedback control. This mode is gentler on both the tip and the sample, making it suitable for softer samples or those prone to damage in contact mode. [5]

5.2.3 Non-contact mode

This mode operates with the tip hovering above the surface without making physical contact. The interaction between the tip and the sample is detected through van der Waals forces. Non-contact mode is suitable for imaging delicate samples and achieving high lateral resolution. [6]

5.2.4 Force Spectroscopy

In force spectroscopy mode, the AFM measures the force between the tip and the sample as the tip is brought into contact and then retracted. This mode provides information about material properties such as elasticity and adhesion. [6]

5.2.5 Quantitative Image Mode

This mode is trademarked by the manufacturer and employs a recording method based on force spectroscopy, where a complete force-distance curve is recorded at each pixel of the image. The AFM tip starts far from the surface, approaches and retracts into the sample until a preset force is reached, and then the tip is withdrawn again. This approach offers a significant advantage in working with living cells under physiological conditions, and when imaging other lateral-force-sensitive samples, providing both simple height data and quantitative information about adhesion or mechanical properties of the sample. The result is high-resolution images with detailed insights into the sample's characteristics. [7]

6 Polymers

Polyethylene Terephthalate (**PET**) falls within the polyester family of polymers and is synthesized from the monomers ethylene glycol and terephthalic acid (or its dimethyl ester, dimethyl terephthalate). The interaction of these monomers, $C_{10}H_8O_4$ yields PET and water. [8] PET stands out as a transparent, robust, and lightweight polymer with commendable dimensional stability and resistance to stretching. Its transparency varies between the amorphous, which is clear, and the crystalline, which is opaque and white. PET demonstrates chemical resistance to mineral acids, bases, and select organic solvents, although it is vulnerable to strong alkalis and specific organic solvents. Possessing high tensile strength and stiffness, PET excels in impact resistance. This versatile polymer finds extensive applications across various industries. [9] In packaging, PET is notably used for producing plastic bottles for beverages and other liquids. Its utility extends to food packaging, encompassing containers and films. Within the textile sector, PET is a prevalent material for manufacturing fibers used in clothing, carpets, and fabrics, often referred to as PET polyester. Additionally, PET is employed in the production of certain medical devices due to its transparency, strength, and sterilizability. [8] PET's recyclability is a noteworthy aspect of its environmental profile. Recycled PET (rPET) is widely utilized in the production of new PET products, aligning with sustainability initiatives. Despite these advantages, PET's chemical resistance poses challenges to biodegradation, necessitating proper recycling practices to address environmental concerns. [10]

High-Density Polyethylene (**HDPE**) is a member of the polyethylene family, distinguished by its elevated molecular weight and density. Its formation involves the polymerization of ethylene monomers (C_2H_4), giving rise to extensive polymer chains. Renowned for its high density, HDPE exhibits notable strength and rigidity, displaying superior tensile strength and stiffness suitable for a variety of structural applications. This polymer demonstrates resilience against numerous chemicals, acids, and bases, enhancing its durability across diverse environments. Additionally, HDPE maintains its properties over a broad temperature spectrum, exhibiting resistance to fluctuations in heat. Widely utilized in packaging materials, such as bottles, containers, and bags, HDPE is favored for its lightweight composition and chemical resistance. Also, HDPE plays a pivotal role in medical applications, contributing to the production of devices and containers due to its chemical stability and ease of sterilization. [9] Emphasizing environmental responsibility, HDPE is recyclable, often employed in the creation of recycled plastic products. While considered eco-friendly owing to its recyclability, improper disposal practices can also potentially contribute to environmental pollution. [11]

Low-Density Polyethylene (**LDPE**), a thermoplastic polymer within the polyethylene family, exhibits distinctive characteristics attributed to its branched molecular structure, resulting in a lower density compared to other polyethylene variants. This branching hinders

the close packing of polymer chains, fostering a more amorphous composition. Produced through the polymerization of ethylene monomers under specific conditions, LDPE's low density is achieved by incorporating branches into its molecular structure during the polymerization process. Renowned for its high flexibility and excellent ductility, LDPE has a translucent appearance, conveying a soft and pliable texture. [9] Widely utilized in the manufacturing of diverse packaging materials like plastic bags, films, and containers, LDPE also finds application in the medical sector for products such as medical devices, tubing, and containers, benefiting from its flexibility and chemical inertness. Recognized for its recyclability, LDPE can be reused to create various plastic products. [12]

Polystyrene (**PS**) stands out as a versatile and extensively utilized thermoplastic polymer within the styrenic polymer family. Its synthesis involves the polymerization of styrene monomers (C_8H_8), frequently employing free radical polymerization. With its amorphous nature, PS lacks a well-defined crystalline structure, enhancing its transparency. While maintaining rigidity and brittleness at room temperature, PS exhibits transparency in its solid state, rendering it apt for applications that prioritize clarity. Various processing techniques, including injection molding, extrusion, and foam extrusion, can be employed with PS. Widely used in the production of disposable packaging materials like food containers, cups, trays, and lids, PS foam, recognized as expanded polystyrene (EPS) or Styrofoam, serves as insulation in construction. [9] Although PS is recyclable, its recycling rate remains relatively low, and the environmental impact of expanded polystyrene foam has raised concerns due to its persistence in the environment. [13]

7 Methodology

7.1 Sample synthesis[7]

7.1.1 Synthesis of nanoparticles

Colloidal solutions of Ag and ZnO were synthesized by pulsed laser ablation in water. In the case of Ag colloid, a silver wafer (purity > 99.9%, GoodFellow, Huntingdon, UK) was placed in a glass beaker filled with 50 mL of deionized water. For the synthesis of ZnO colloids, a ZnO ceramic wafer was also placed in a glass beaker filled with 25 mL of deionized water (purity > 99.9%, GoodFellow, Huntingdon, UK). The laser beam is focused on the target using a cylindrical concave lens with a focal length of 10 cm. The angle of incidence of the laser beam is 90°. In the ablation process, a Nd:YAG (Quantel, Brilliant, Les Ulis, France) laser was used with an output wavelength and pulse energy of 1064 nm and 300 mJ, respectively. The duration and repetition of the pulse were 5 ns and 5 Hz, while in the case of Ag the ablation time was 16 min and 40 s while in the case of ZnO it was 10 min.

7.1.2 Synthesis of HDPE/Ag and PET/ZnO composites

The polymers used were HDPE and PET with dimensions (2 x 2) cm^2. In the first step, the polymers were processed using an atmospheric pressure plasma jet (APPJ) (Figure 22). The APPJ consists of: one electrode (copper wire) with a diameter of 0.15 mm, a source of high rectangular voltage, working gas, a gas flow meter and a glass capillary tube. The electrode is located in a borosilicate glass tube with a length of 75 mm and an outer diameter of 1.5 mm. The working gas used was argon and the flow was set via a flow meter (Cole-Parmer, Vernon Hills, IL, USA) at 1 slm[8] while the treatment duration was 2 min. The voltage and frequency used were 10 kV and 10 Hz, and the working distance between the polymer and the jet was 0.5 cm. After the treatment of HDPE with APPJ, 100 μL and 300 μL of Ag colloid was applied. After drying, HDPE with Ag nanoparticles was again treated with APPJ with the same specified parameters. In the case of PET polymer, the procedure is the same except that after treatment with APPJ, 200 μL, 500 μL and 1000 μL of ZnO colloidal solution was applied.

7.2 SEM sample preparation and measurements

SEM is a powerful technique for studying the surface morphology of materials at high resolution. The preparation of polymer specimens for SEM analysis involves careful mounting

[7]Samples were synthesized by Rafaela Radičić from the Institute of Physics in Zagreb and she contributed to the final version of this text.

[8]standard liter per minute

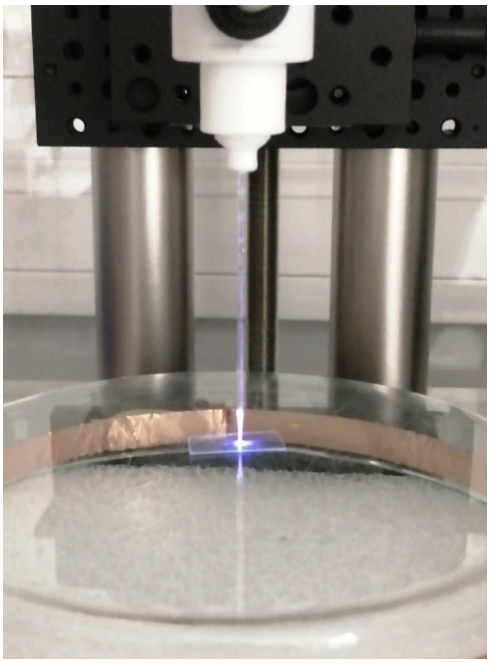

Figure 22: *Experimental presentation of polymer treatment with APP.*

to ensure proper conductivity and minimize charging effects. This section outlines the experimental setup designed for the preparation of polymer samples on SEM stubs.

Polymer specimens are manipulated using tweezers, precisely sectioned into appropriate dimensions with specialized tools, and subsequently positioned onto SEM stubs. Next, fragments of carbon tape are meticulously cut and delicately affixed to the polymer specimen, ensuring secure adhesion to the SEM stub. Any surplus carbon tape is then removed to achieve a tidy presentation. Additionally, a modest quantity of carbon paste is dispensed onto a clean surface and applied using a spatula to the junction between the polymer specimen and the carbon tape. This process guarantees uniform coverage, establishing effective electrical contact. The mounted specimens are allowed to undergo thorough drying, ensuring the solidification of the carbon paste. When the sample is ready, a thin layer of platinum (2 nm) is sputtered onto it using the sputter coater. The working principle of the sputter coater is described in section 4 and samples adequately prepared for SEM examination are shown in Figure 23.

To prepare the sample for SEM examination, the stub is securely affixed to the sample holder and subsequently introduced into the pre-chamber. The pre-chamber then needs to be evacuated which is done with a vacuum pump. Upon reaching an adequate vacuum level, the valve connecting the pre-chamber to the main chamber is opened, allowing the sample to be inserted using a lever. The specimen is then positioned for examination by establishing a working distance (WD), specimen tilt and other operational parameters. Once the configuration is complete, the electron gun is activated to generate an image of the sample. Image refinement involves utilizing a focus knob, and for significant magnifications, adjusting the x- and y-axis

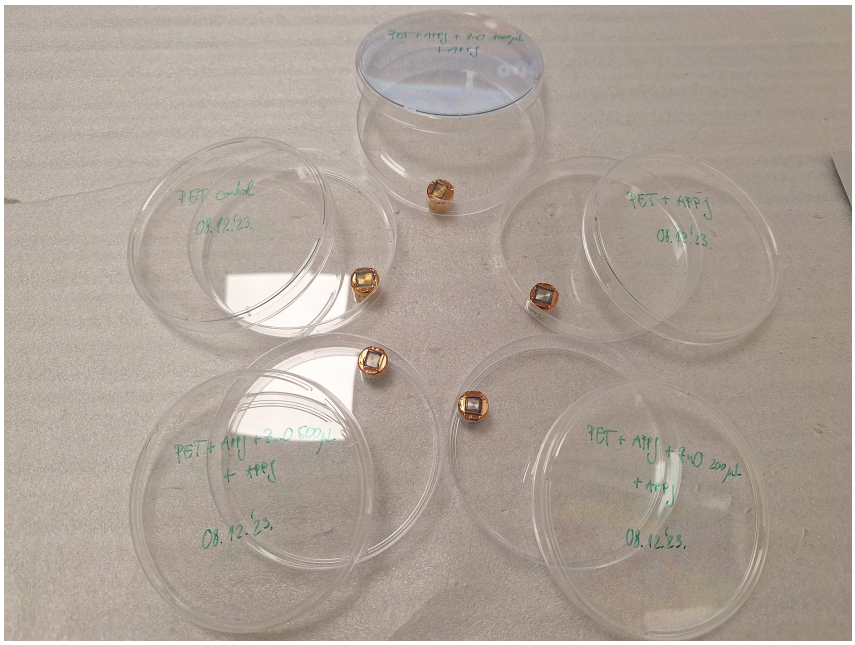

Figure 23: *PET samples adequately mounted onto subs and coated with platinum using the sputter coater.*

knobs to regulate astigmatism. Also, brightness and contrast adjustments are available.

First we examined the non-treated control polymer samples (PET, HDPE, PS and LDPE). This step was especially important and time-costly since it involved research on optimal SEM imaging parameters. We then treated samples of PET and HDPE. HDPE treated samples included: HDPE processed using an atmospheric pressure plasma jet (**HDPE+APPJ**); HDPE processed using APPJ and then 100 μL Ag colloid was applied, which was again treated with APPJ (**HDPE+APPJ+Ag100+APPJ**); HDPE processed using APPJ and then 300 μL Ag colloid was applied, which was again treated with APPJ (**HDPE+APPJ+Ag300+APPJ**).

PET treated samples included: PET processed using an atmospheric pressure plasma jet (**PET+APPJ**); PET processed using APPJ and then 200 μL ZnO colloid was applied, which was again treated with APPJ (**PET+APPJ+ZnO200+APPJ**); PET processed using APPJ and then 500 μL ZnO colloid was applied, which was again treated with APPJ (**PET+APPJ+ZnO500+APPJ**); PET processed using APPJ and then 1000 μL ZnO colloid was applied, which was again treated with APPJ (**PET+APPJ+ZnO1000+APPJ**).

Samples were examined with respect to sensitivity of polymer surfaces under SEM, using low accelerating voltage of 1.50 kV and low probe current of 7 μA. The column mode was set on Gentlebeam-High with r-filter SB and Upper Electron Converter (UEC) inserted. UEC is an electrode that collects low-energy electrons that escape the r-filter. Working distances were between 3 and 5 mm and tilt was between 11° and 15°.

Energy-dispersive X-ray spectroscopy (EDS) is conducted using a separate detector, as detailed in the section 3. After positioning the detector, parameters such as working distance,

beam current, beam voltage, and width are configured to achieve a desired dead time (a percentage indicating the proportion of unprocessed X-rays).

Samples were examined without tilt and with greater WD (around 15 mm) in SEM column mode, without UEC inserted. Probe current was elevated to 13 μA and accelerating voltage was set to 3 kV for PET and 6 kV for HDPE (with respect to their L_{alpha} lines).

7.3 AFM measurements

All AFM samples were glued onto a glass slide and image in air at ambient temperature. AFM measurements were performed with a Nanowizard IV (JPK/Bruker, CA, USA) in AC mode or quantitative imaging (QITM) using TESPA-V2 and RTESPA probes (Bruker, CA, USA). Data were obtained in areas of 5 μm $\times$ 5 μm with a resolution of 512 $\times$ 512 pixels and a scan rate of up to 1.5 Hz. For QI measurements, force setpoint was kept up to 7 nN. Data processing and visualization was performed using JPK data processing software. All data were plain fitted after which a first order polynomial fit was subtracted from each scan line independently. From such data, surface roughness parameters were calculated in Gwyddion. These parameters were calculated from 5 different data sets (images).

7.4 Antibacterial activity

To evaluate the antibacterial efficacy, the synthesized surfaces were tested against the representative biofilm-forming strain *Staphylococcus aureus* ATCC 25923. The test procedure was a modification of ISO standard 22196. [14] The procedure was as follows. A 20 μL aliquot of cells in glycerol broth (-80 °C) was transferred to 3 mL of freshly prepared Mueller-Hinton broth[9] (MHB, Biolife, Italy) and incubated for 18 hours at 37 °C with shaking at 220 rpm. The next day, the resulting culture was diluted 50-fold in fresh MHB and left to reach the exponential growth phase at 37 °C and 220 rpm shaking (about two hours). In the meantime, the synthesized surfaces were placed under UV light for 2 hours for disinfection and then transferred to sterile Petri dishes. All surface manipulations and treatments were performed in a safety cabinet.

After the cells had reached the exponential growth phase, their concentration was determined spectrophotometrically and adjusted to 5×10^5 CFU/ml by diluting the culture in fresh MHB. At this point, 30 μL of this culture was added to the synthesized surfaces. To prevent evaporation, each sample was covered with pieces of Parafilm sterilized with 70% EtOH and air-dried. Finally, the prepared samples were transferred to the incubator set at 37 °C with 90% relative humidity for 24 hours. The samples were done in duplicates. The prepared sample of PET

[9]Mueller-Hinton broth is a nutrient-rich liquid medium commonly used for the cultivation of bacteria for various purposes.

pure is shown in Figure 24. After 24 hours of incubation, the parafilm covers were carefully removed and the entire polymer sample was immersed in fresh MHB and shaken for a few seconds, resulting in a 200-fold dilution of the starting inoculum. This dilution was then further diluted to give a 2000-fold and a 20000-fold dilution. Aliquots of 10 μL of these cultures were then plated onto freshly prepared MHB agar plates and incubated for 24 hours. Every prepared sample was plated on two agar plate resulting in 4 agar plates per polymer surface. Cultures of PET pure sample are shown in Figure 25. While presuming that each bacterium is a colony-forming unit, we counted the number of colonies on each plate the next day. If the synthesized surfaces have an antibacterial property, it is expected that the bacteria growing on the nanoparticle-enhanced surfaces should be reduced.

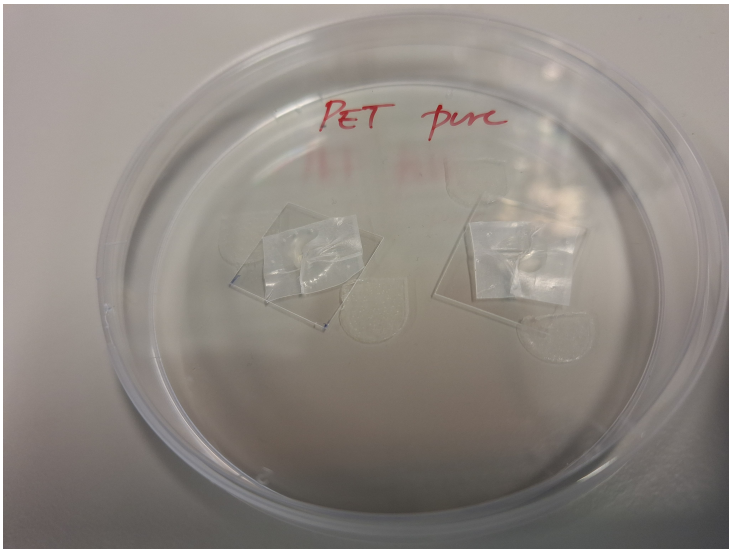

Figure 24: *The prepared sample of PET pure.*

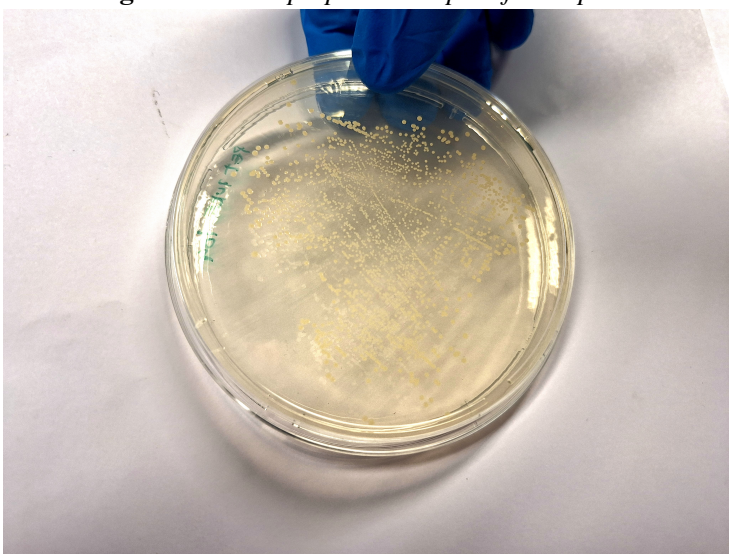

Figure 25: *S. aureus CFU grown on pure PET samples.*

8 Results

8.1 SEM imaging and EDS spectra

Figure 26 illustrates control samples of PET, HDPE, LDPE, and PS. As anticipated, the polymer morphologies align with the descriptions provided in section 6. PS exhibits a remarkably smooth surface, devoid of polymer threads as in HDPE samples, with a subtle irregularity likely stemming from the polymer's rolling during production. PET showcases some irregularities, whereas both HDPE and LDPE exhibit well-defined morphological characteristics. The surface roughness of HDPE results from its extensive polymer chains, whereas LDPE, despite sharing the same molecular structure, displays lower density due to its branched configuration.

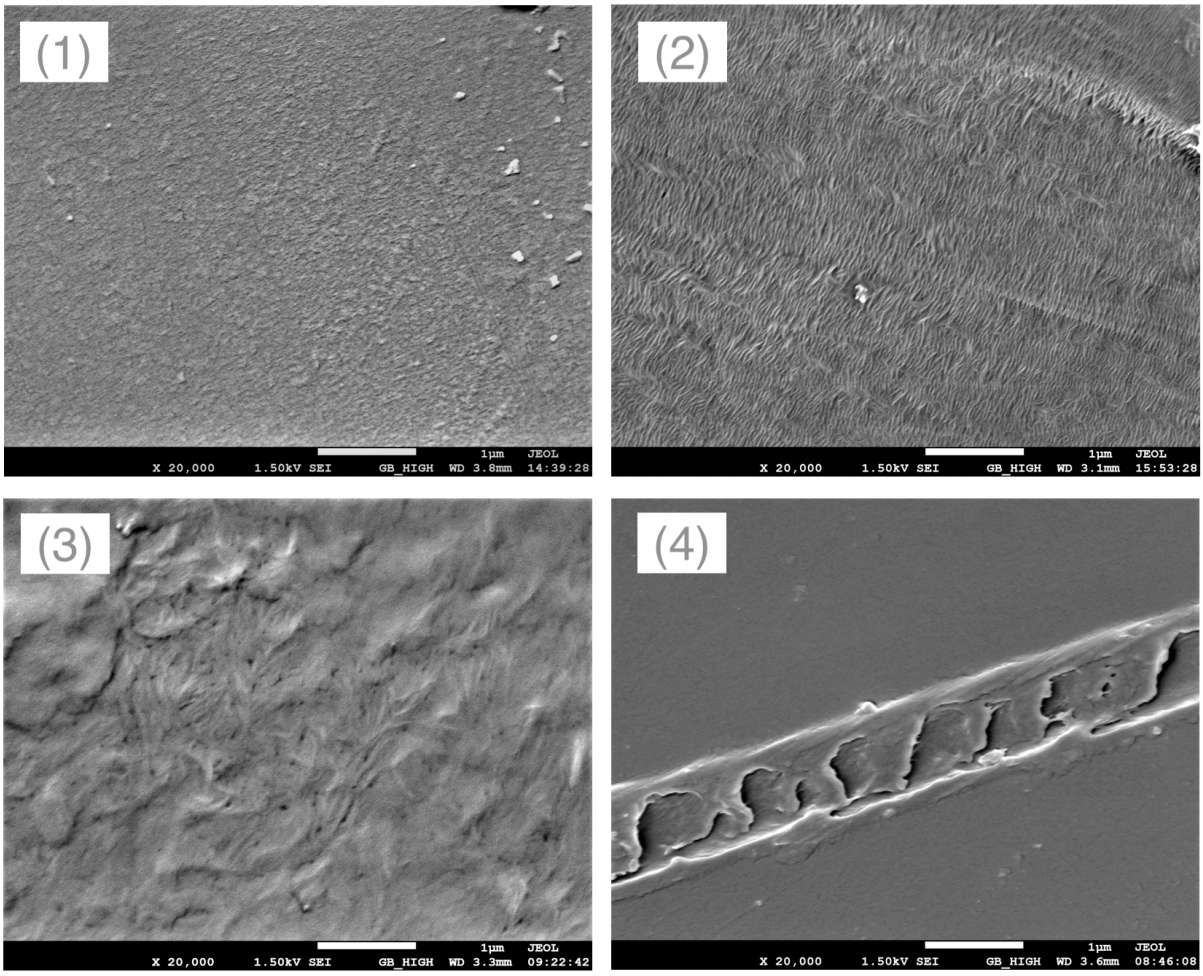

Figure 26: *SEM image of control polymer samples: (1) PET, (2) HDPE, (3) LDPE and (4) PS.*

Figure 27 showcases samples of HDPE polymer, where the already substantial surface morphology is further intensified through treatment with APPJ. Notably, nanoparticles exhibit a grouping phenomenon, forming both larger and smaller clusters. As anticipated, the surface with a higher colloid concentration exhibits an increased density of nanoparticles.

Figure 28 displays the PET samples, revealing more roughness of surface upon treatment

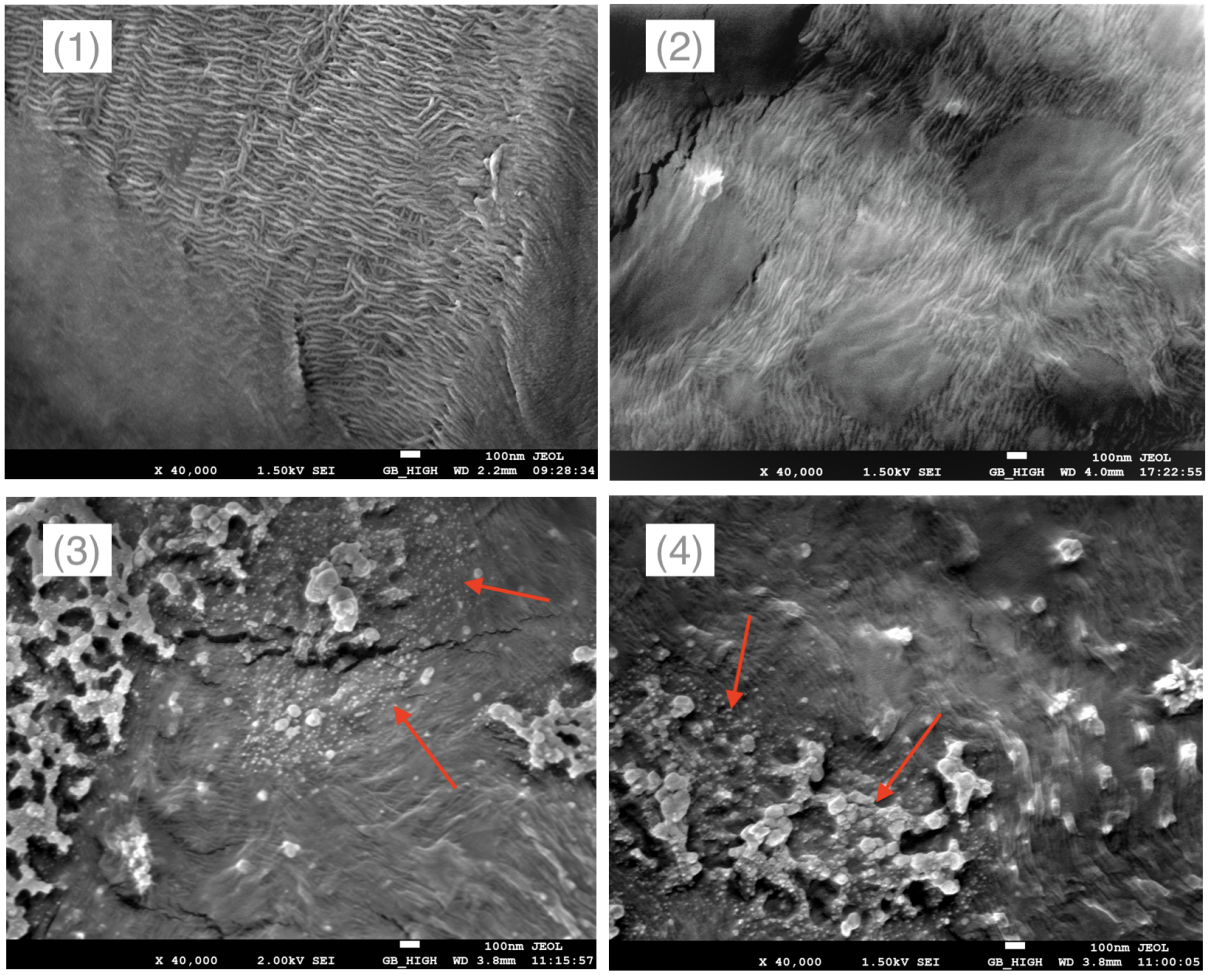

Figure 27: *SEM image of HDPE polymer samples (1) HDPE, (2) HDPE+APPJ, (3) HDPE+APPJ+Ag100+APPJ, (4) HDPE+APPJ+Ag300+APPJ. Clusters of nanoparticles are marked with red arrows.*

with APPJ. The enhancement of samples with varying concentrations of ZnO colloid induces a discernible alteration in surface roughness. Notably, nanoparticles become increasingly prominent, correlating with the elevated concentration of the colloid. SEM images show that the ZnO nanopartcles surpass the size of Ag nanoparticles.

Figures 29 and 30 present the EDS results for HDPE and PET samples, respectively. The HDPE spectrum distinctly reveals the presence of ethylene monomers (C_2H_4), evidenced by the percentage of carbon, and also platinum coating. Hydrogen is not detectable by EDS. Notably, silver is exclusively detected on the enhanced HDPE sample. Similarly, the PET spectrum reflects its monomers ($C_{10}H_8O_4$), with a significant representation of carbon and oxygen atoms, along with a thin platinum coating. In the enhanced PET spectrum, the presence of ZnO colloid is clearly visible.

The percentage of atoms in each spectrum is shown in Table 1.

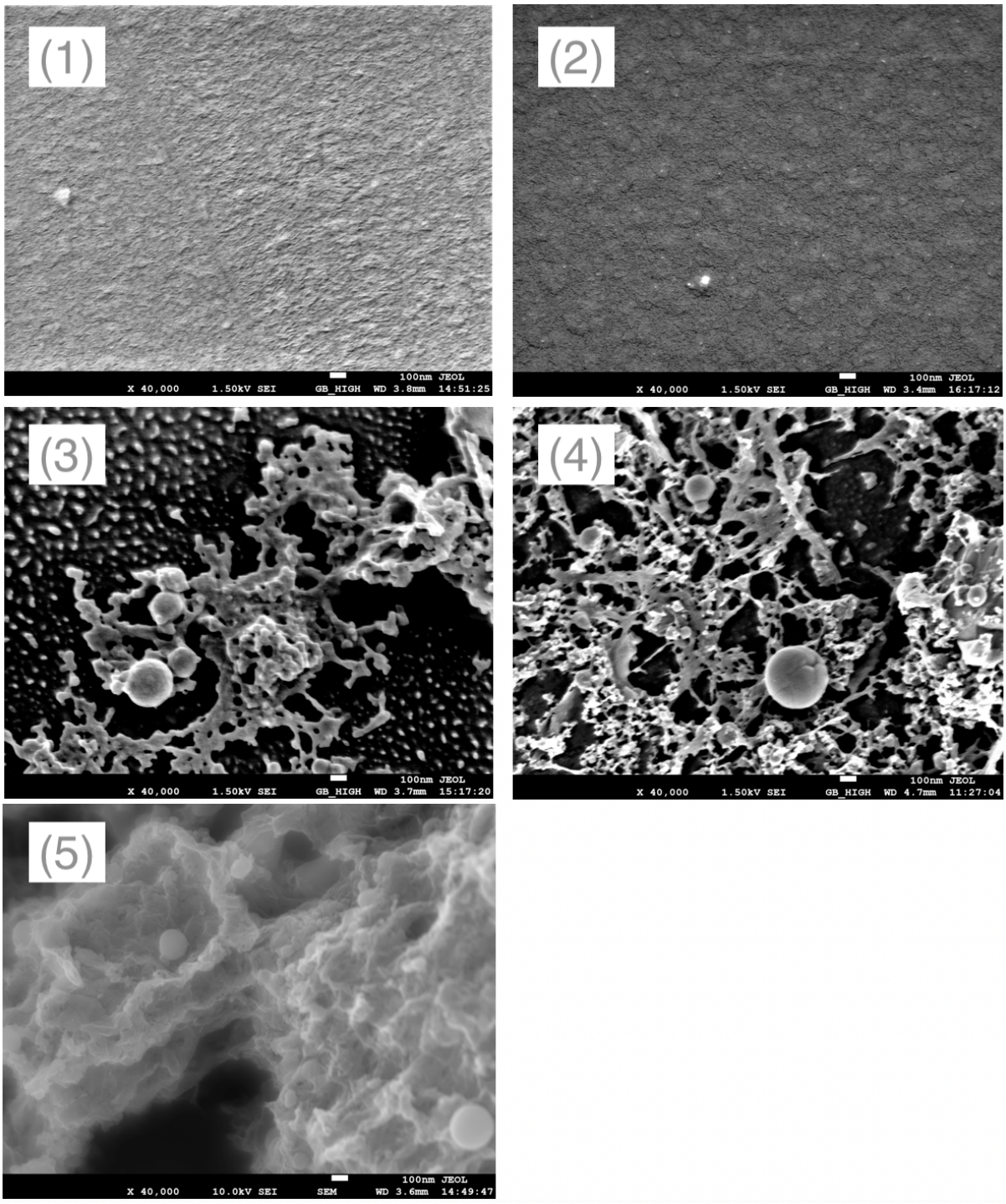

Figure 28: *SEM image of PET polymer samples (1) PET, (2) PET+APPJ, (3) PET+APPJ+ZnO200+APPJ, (4) PET+APPJ+ZnO500+APPJ, (5) PET+APPJ+ZnO1000+APPJ.*

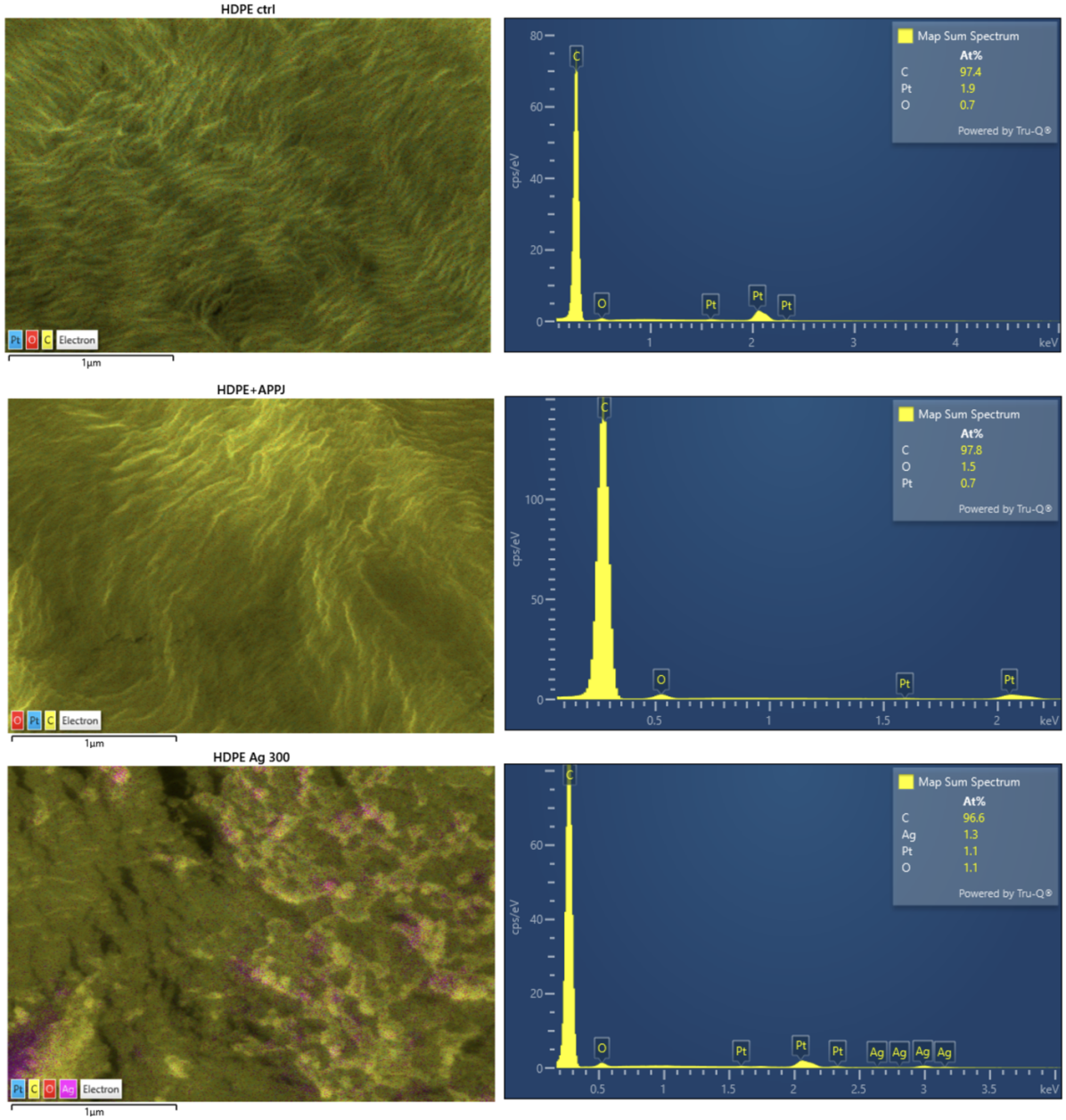

Figure 29: *Spectrum of HDPE pure, HDPE+APPJ and HDPE+APPJ+Ag300+APPJ with corresponding SEM images showcasing the disribution of atoms in color scheme.*

	C(%)	O(%)	Pt(%)	Ag(%)	Zn(%)
HDPE pure	97,40	0,70	1,90	/	/
HDPE+APPj	97,80	1,50	0,70	/	/
HDPE+APPj+Ag300+APPJ	96,60	1,10	1,10	1,30	/
PET pure	84,70	14,60	6,00	/	/
PET+APPj	86,20	10,30	3,50	/	/
PET+APPj+ZnO1000+APPJ	78,50	15,50	1,30	/	4,70

Table 1: *The percentage of atoms in each spectrum.*

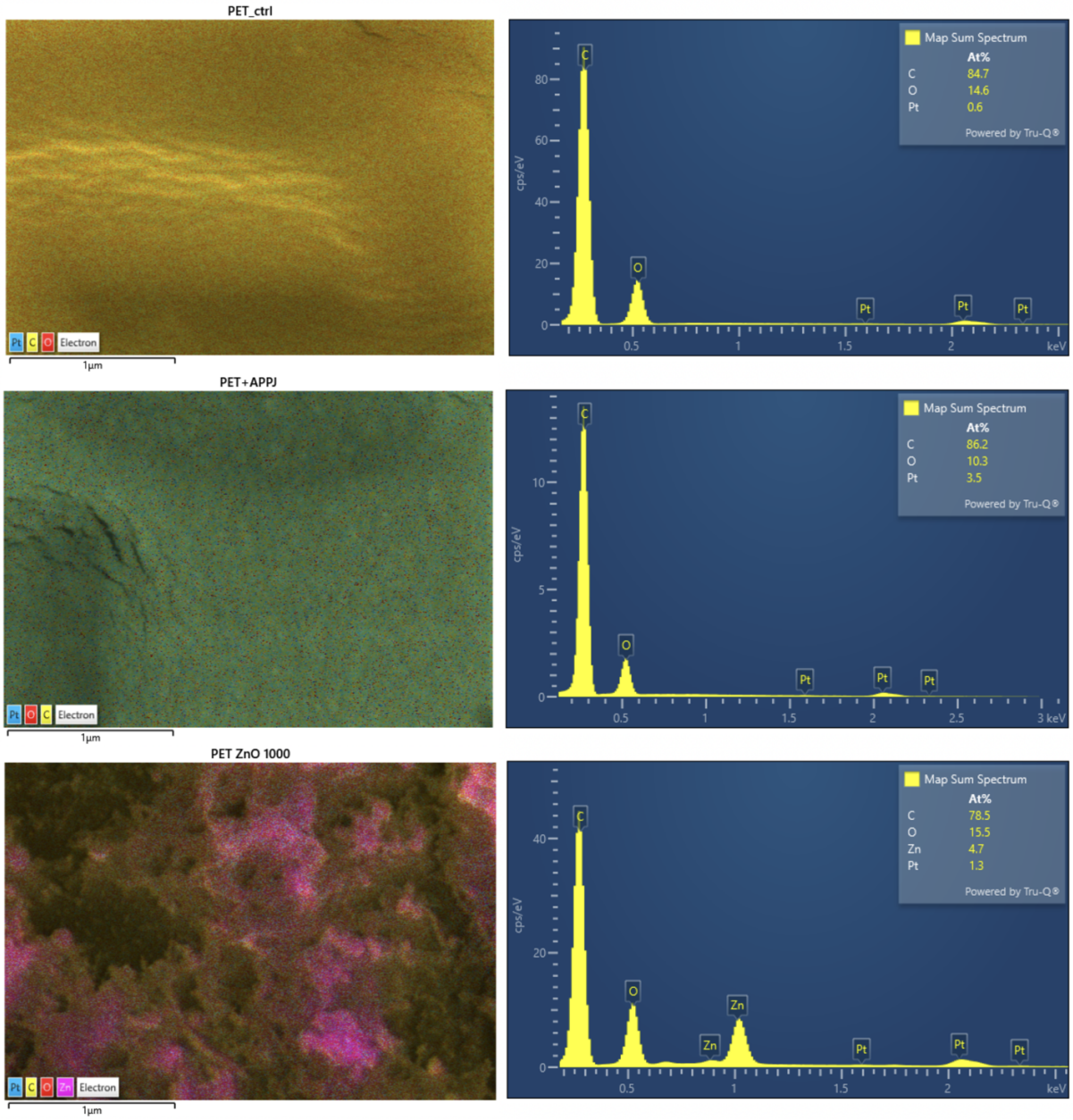

Figure 30: *Spectrum of PET pure, PET+APPJ and PET+APPJ+ZnO1000+APPJ with corresponding SEM images showcasing the distribution of atoms in color scheme.*

8.2 AFM imaging

Side by side comparison of HDPE pure and HDPE+APPJ AFM images in Figure 31 vividly demonstrate the impact of APPJ on surface roughness. In the enhanced samples, there is noticeable visibility of nanoparticles and their clustering.

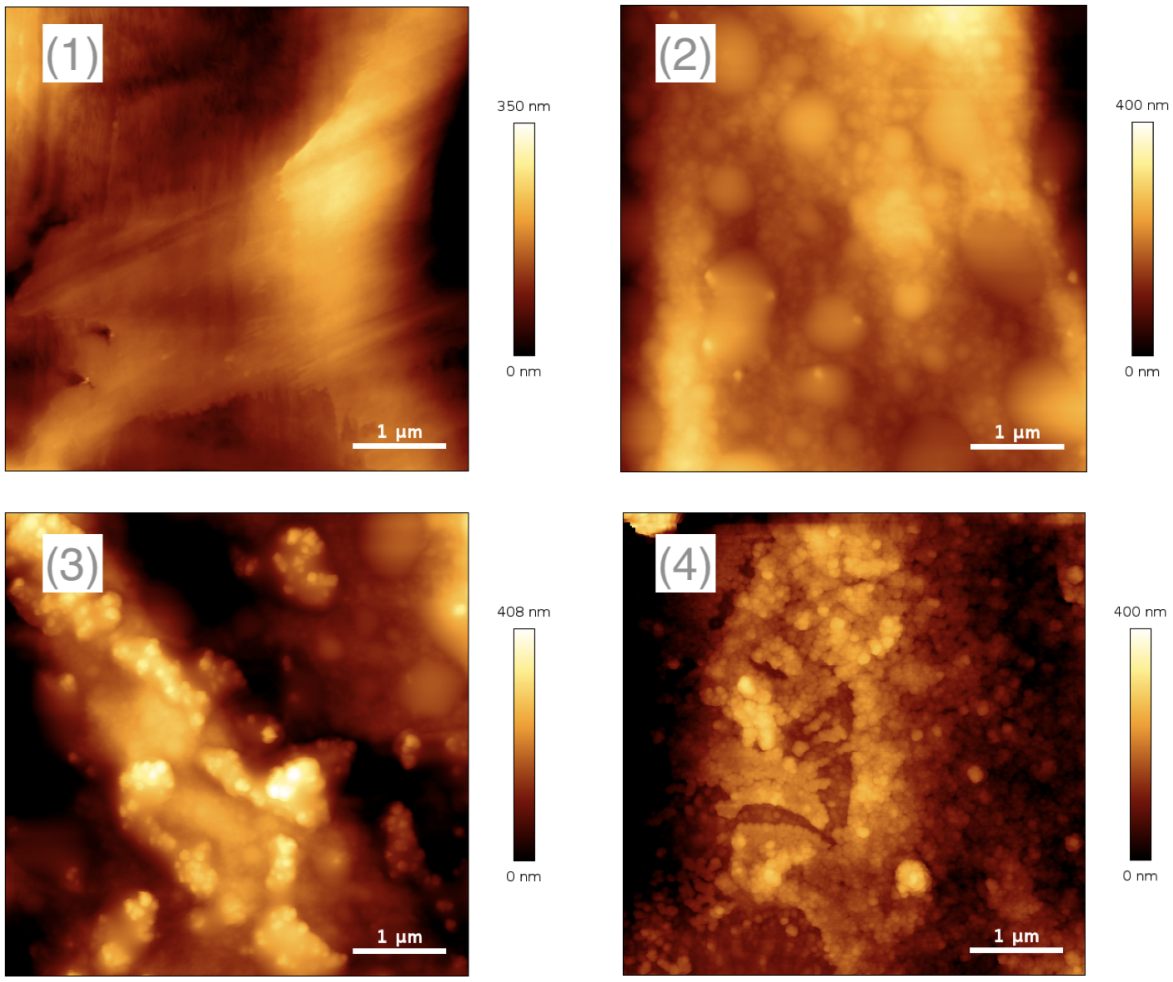

Figure 31: *AFM image of HDPE polymer samples (1) HDPE pure, (2) HDPE+APPJ, (3) HDPE+APPJ+Ag100+APPJ, (4) HDPE+APPJ+Ag300+APPJ.*

Only AFM images of PET pure and PET+APPJ could be obtained and they are in accordance with our initial ideas when treating samples with APPJ, meaning they revealed small, if any, alteration of PET surfaces after APPJ treatment (Figure 32). Images of enhanced samples could not be obtained because the surface was too adhesive to be measured and the AFM probe did not work correctly.

Two parameters used to determine roughness of our samples were mean roughness, R_a, defined as

$$R_a = \frac{1}{N}\sum_{n=1}^{N}(z_n - \overline{z}), \tag{8.1}$$

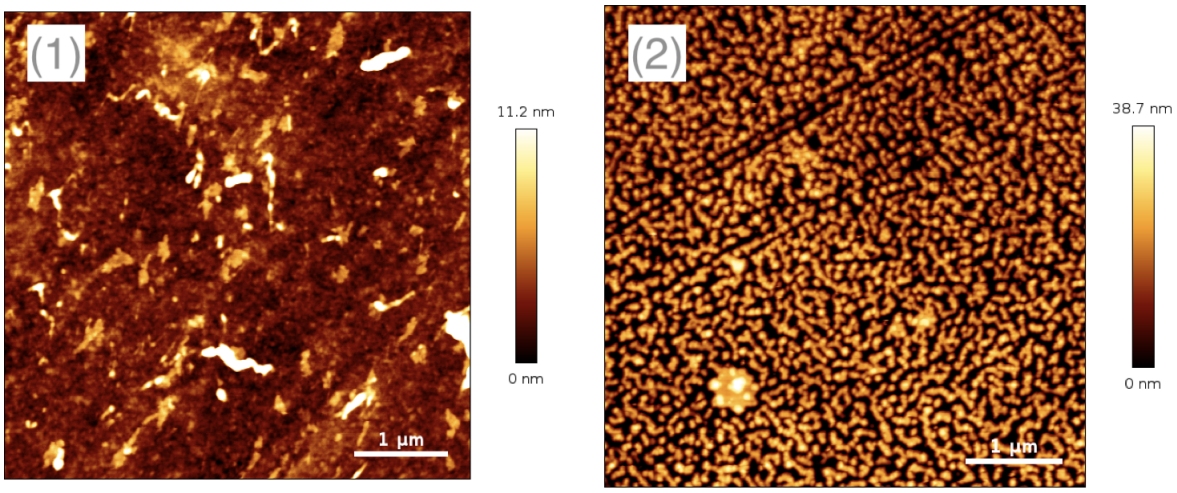

Figure 32: *AFM image of PET polymer samples (1) PET pure and (2) PET+APPJ.*

where N represents the number of pixels, z_n the height measured at n pixel, and $\overline{z}$ the mean height and root mean square roughness, R_q, defined as

$$R_q = \sqrt{\frac{1}{N}\sum_{n=1}^{N}(z_n - \overline{z})^2}. \tag{8.2}$$

The table in Figure 33 shows the RMS roughness for each HDPE sample.

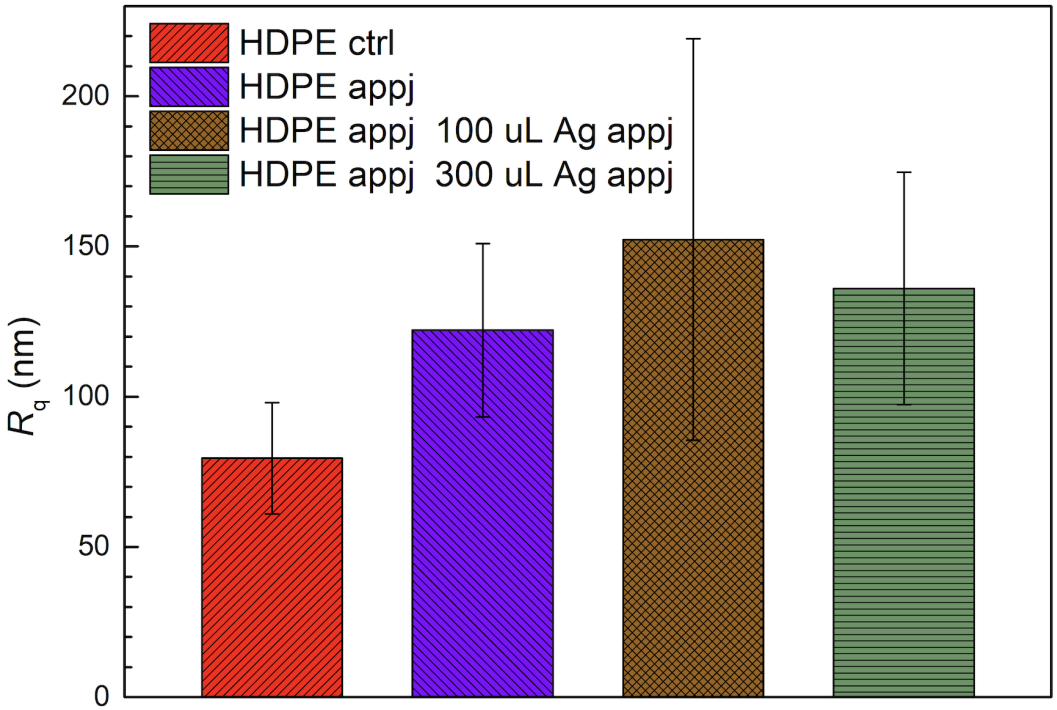

Figure 33: *RMS roughness, R_q, shown for each HDPE sample.*

Detailed results are presented in Table 2. Notably, measured roughness of the sample with the highest Ag concentration was unexpectedly low., i.e. it does not follow the roughness increase trend. This could be due to undersampling of the surface. Therefore, additional measurement should be performed.

	R_a [nm]	R_q [nm]
HDPE pure	61,05 $\pm 15,15$	79,51 ± 18.57
HDPE+APPj	97,63 $\pm 30,53$	122,11 $\pm 28,83$
HDPE+APPj+Ag100+APPJ	126,67 $\pm 58,35$	152,30 $\pm 66,77$
HDPE+APPj+Ag300+APPJ	108,08 $\pm 32,26$	136,04 $\pm 38,64$
PET pure	5,03 $\pm 0,39$	6,00 ± 0.46
PET+APPj	10,30 $\pm 1,87$	13,49 $\pm 3,77$

Table 2: *Mean roughness, R_a, and RMS roughness, R_q, calculated for each sample.*

8.3 Measuring the antibacterial effect

In Table 3 we see the measured normalized colony-forming unit reduction for each sample. APPJ treated and nanoparticle-enhanced samples are normalized by averaging their CFU number over the CFU number of control samples, i.e., HDPE pure and PET pure. It can bee seen that the relative CFU number generally reduces with the increasing concentration of nanoparticles. This is a positive sign, although our results for antibacterial effect are far from satisfactory.

	Normalized CFU reduction
HDPE pure	100,00%
HDPE+APPj	78,85%
HDPE+APPj+Ag100+APPJ	90,84%
HDPE+APPj+Ag300+APPJ	15,49%
PET pure	100,00%
PET+APPj	135,78%
PET+APPj+ZnO200+APPJ	51,80%
PET+APPj+ZnO500+APPJ	57,49%
PET+APPj+ZnO1000+APPJ	20,37%

Table 3: *Normalized CFU reduction.*

9 Conclusion

By imaging the samples with SEM, we could successfully see the morphology of the pure samples as well as the morphology changes that the samples underwent with plasma jet treatment and enhancement with nanoparticles. The main difficulties in SEM imaging arose due to the non-conductivity and smoothness of the samples themselves. For this reason, we coated the samples with platinum and performed measurements with low accelerating voltage. Despite these improvements, imaging had to be done quickly and accurately due to the inherent sensitivity of the samples. By further studying the prepared PET and HDPE polymers, which were treated with APPJ and enhanced with nanoparticles, we noticed a real increase in surface roughness after plasma jet treatment, and we successfully imaged zinc oxide and silver nanoparticles on SEM. We determined the composition of these various samples by EDS analysis, and the spectra agreed with our initial thesis. In addition, we measured the surface roughness (average and RMS roughness) with AFM and saw the success of all surface treatment techniques. We were unable to measure the surfaces of PET enhanced with nanoparticles with AFM due to excessive surface adhesion. The final analysis was to check the assumed antibacterial effect. By growing *S. aureus* bacteria on unmodified and modified polymers, we saw that there is a certain antibacterial effect in samples improved with colloids, but not in a satisfactory amount. Further research would focus on nanoparticle surface distribution issues, since we saw in our research that nanoparticles gather in clusters, and improvement of the antibacterial effect and its testing protocol. Likewise, AFM imaging would have to be achieved for the PET sample treated with ZnO colloid.

10 Bibliography

[1] Anwar Ul-Hamid: *A Beginners' Guide to Scanning Electron Microscopy*, Springer, 2018

[2] Jeol instruction manual: *JSM-761OFPlus, Field Emission Scanning Electron Manual*, 2019.

[3] Jeol Analytical and Imaging Solutions for Advanced: *Gentle Beam: Improving low voltage performance*

[4] Stephen Swan: *Magnetron sputtering*, Physics in Technology, 1988.
URL: https://dx.doi.org/10.1088/0305-4624/19/2/304

[5] Peter Eaton, Paul West: *Atomic Force Microscopy*, Oxford University Press, 2010

[6] JPK Instruments: *NanoWizard AFM*, Handbook, Version 6.0 – 07/2018

[7] QI tm mode: *Quantitative Imaging with the NanoWizard 3 AFM*

[8] Lobke De Vos, Babs Van de Voorde, Lenny Van Daele, Peter Dubruel, Sandra Van Vlierberghe: *Poly(alkylene terephthalate)s: From current developments in synthetic strategies towards applications*, European Polymer Journal, Volume 161, 2021.
URL: https://doi.org/10.1016/j.eurpolymj.2021.110840

[9] James M. Margolis: *Engineering Thermoplastics: Properties and Applications*, CRC Press, 2020.

[10] Neetu Malik, Piyush Kumar, Sharad Shrivastava, Subrata Bandhu Ghosh: *An overview on PET waste recycling for application in packaging*, Int J Plast Technol 21, 1–24, 2017.
URL: https://doi.org/10.1007/s12588-016-9164-1

[11] Industrial Plastics: *HDPE Plastic (High Density Polyethylene)*
URL: https://industrialplastics.com.au/hdpe-plastic-high-density-polyethylene/

[12] Plastic Expert: *LDPE Recycling*
URL: https://www.plasticexpert.co.uk/plastic-recycling/ldpe-recycling-plastic/

[13] Emad Yousif, Raghad Haddad:*Photodegradation and photostabilization of polymers, especially polystyrene: review*, Springerplus, 2013.
URL: doi:10.1186/2193-1801-2-398

[14] Technical Guidance Operating Procedures in Life Sciences: *ISO 22196, Adapted Test Protocol*.
URL: http:
//myweb.sabanciuniv.edu/emrehakli/in-microbiology/iso-22196-adapted-test-protocol/